# Search for unidentified Terrestrial Gamma-ray Flashes

Master Thesis in Space Physics

by
Kjetil Haakonseth Albrechtsen


Department of Physics and Technology
University of Bergen
Norway

"All things are difficult before they are easy"

- Dr Thomas Fuller (1608– 1661)

# Acknowledgements

This is the product of many long hours and late nights working at the university, and I am both proud and relieved to complete it. The work has been hard, but also rewarding due to the great feeling of accomplishment upon completion. I would like to thank my supervisors Nikolai Østgaard and Thomas Gjesteland, who have gone above and beyond my expectations when it comes to their help and guidance for this thesis.

I also wish to thank the World Wide Lightning Location Network, a collaboration among over 50 universities and institutions, for providing the lightning location data used in this paper. In addition, I would like to thank all members of the RHESSI project for the provided data.

I am also thankful for the other master students here, Vegard, Markus, Stefan, Anders, Theresa, Norah and Annet Eva. Not only for the valuable help they have provided me, but also for the comradery between us.

Finally I would like to thank my friends Paul, Chris and Mariano who have been a great help in rubber duck debugging and keeping my motivation up.

Kjetil Haakonseth Albrechtsen

01/06/2015

# Abstract

Terrestrial Gamma-ray Flashes (TGFs) are the most energetic natural phenomena on Earth with possible energies above 40MeV. They consist of large amounts of energetic photons ($\sim 10^{17} - 10^{19}$) produced in thunderstorms at 15-21km altitude. It is still an open question how often they occur and the exact production mechanisms for them.

In this thesis we will use data from the World Wide Lightning Location Network (WWLLN) and the satellite RHESSI to investigate if there are fainter TGFs in existence that has yet to be identified. We will do this by extracting the light curves from RHESSI at the time of each WWLLN registered lightning flash in 2006 and 2012, and superpose these to see if there is a statistical increase in registered counts at the time of lightning. We discarded every lightning flash happening outside of RHESSI's field of view, and corrected for the travel time of gamma-rays to the satellite, as well as correcting for the systematic error in RHESSI's internal clock.

We found that there is a statistical increase in counts at the time of lightning, with an increase of $\sigma = 5.0$ assuming a Poisson distribution. This indicated that there are weaker TGFs in existence that currently cannot be distinguished from the background.

Further on we attempted to fit the fluence distribution of these possible weak TGFs to a power law, as has been suggested by *Østgaard et al.* [2012] and found that the exponent $\lambda = 1.82$.

This is consistent with *Østgaard et al.* [2012] proposed hypothesis of a roll off at the lower end of the fluence distribution of TGFs, and supports the hypothesis that all lightning produce (or are associated with) TGFs.

# List of Abbreviations

| | |
|---|---|
| **+CG** | Positive Cloud to Ground (lightning flash) |
| **+IC** | Positive Intra Cloud & Inter Cloud (lightning flash) |
| **-CG** | Negative Cloud to Ground (lightning flash) |
| **-IC** | Negative Intra Cloud & Inter Cloud (lightning flash) |
| **ADELE** | Airborne Detector for Energetic Lightning Emission |
| **AGILE** | Astrorivelatore Gamma a Immagini LEggaro (a satellite) |
| **ATD** | Arrival Time Difference |
| **BATSE** | Burst and Transient Source Experiment (instrument on CGRO) |
| **CG** | Cloud to Ground (lightning flash) |
| **CGRO** | Compton Gamma Ray Observatory (NASA satellite) |
| **ECI** | Earth-centred Inertial (a coordinate system) |
| **FOV** | Field of View |
| **GBM** | Gamma-ray Burst Monitor |
| **GRB** | Gamma-Ray Bursts |
| **IC** | Intra Cloud & Inter Cloud (lightning flash) |
| **LAD** | Large Area Detector |
| **LASA** | Los Alamos Sferic Array |
| **LIS** | Lightning Imaging Sensor |

| | |
|---|---|
| **LP** | Lower Positive (charge centre) |
| **MF** | Medium Freqyency (radiowaves) |
| **MN** | Main Negative (charge centre) |
| **REA** | Runaway Electron Avalanche |
| **RHESSI** | Reuven Ramaty High Energy Solar Spectroscopic Imager (NASA satellite) |
| **RREA** | Relativistic Runaway Electron Avalanche |
| **SAA** | South Atlantic Anomaly |
| **SD** | Spectroscopy Detector |
| **TGF** | Terrestrial Gamma-ray Flash |
| **TOA** | Time Of Arrival |
| **TOGA** | Time Of Group Arrival |
| **TRMM** | Tropical Rainfall Measuring Mission |
| **UP** | Upper Positive (charge centre) |
| **UTC** | Coordinated Universal Time (from Temps Universel Coordonne) |
| **VLF** | Very Long Frequency (radiowaves) |
| **WWLLN** | World Wide Lightning Location Network |

# Contents

# Chapter 1

# Introduction

Terrestrial Gamma-ray flashes are bursts of high energy gamma-rays first discovered in 1991 by the Burst and Transient Source Experiment (BATSE) [*Fishman et al.*, 1994], an instrument on the Compton Gamma Ray Observatory (CGRO) satellite.

BATSE was originally designed for detecting gamma-ray bursts from other galaxies. In addition to this researchers noticed flashes of gamma-rays, shorter than the expected bursts, coming from the earth itself. Over two years BATSE detected only around 12 of these TGFs and *Fishman et al.* [1994] argued that this was due to the relatively long trigger time of BATSE compared to the very short duration of TGFs. This means that BATSE could only detect very strong TGFs (i.e. many incident gamma-rays).

In 2002 RHESSI (Reuven Ramaty High Energy Solar Spectroscopic Imager) was launched by NASA. RHESSI is a smaller instrument than BATSE, but has a much larger energy range, and the ability for data to be downloaded and later searched with algorithms on the ground. As a result, RHESSI was able to detect a TGF roughly every 2.4 days in the first few years of its operation [*Grefenstette et al.*, 2009]. RHESSI also managed to determine that TGFs do in fact have their origin from thunderstorms. Specifically that they originate from positive intra cloud lightning (lightning happening upwards inside a cloud) [*Cummer et al.*, 2005] at an altitude of around $\sim$20km [*Dwyer and Smith*, 2005].

In 2012, *Østgaard et al.* [2012] suggested that the true fluence distribution at

satellite height might be higher than the current level of detectable TGFs and argued that with improved detection algorithms and more sensitive instruments we should be able to detect more TGFs. They suggested that maybe every lightning flash is associated with a TGF, but we lack the instruments to adequately detect them. They suggested that TGFs follow a power law of the form $f(x) = Ax^{-\lambda}$ where $A$ is a scaling constant, and $\lambda$ describes the slope of the fluence distribution of TGFs. They found that $\lambda = 2.3$ if there is a sharp cut off in the fluence distribution, and 1.7 if there is a roll off at the low end of the fluence distribution. Our goal for this thesis is to determine if there are faint TGFs in existence, and if so, how does this distribution fit to a power law?

This project uses data from the World Wide Lightning Location Network (WWLLN), a system that accurately can determine the time and the location (in longitude and latitude) of lightning discharges. We also have data from the satellite RHESSI, where we can extract light curves (a plot showing the brightness of incoming high energy photons, seen in Figure 3.2 ) at the time of lightning flashes.

All lightning strikes outside of RHESSI's field of view will be discarded as the produced gamma-rays will not be able to reach the satellite. We have access to WWLLN data from the years 2006 and 2012.

We have superimposed the light curves from all the lightning flashes that RHESSI can detect gamma-rays from (excluding already known TGFs) to see if there is a statistical increase in gamma-rays at the time of lightning. We found that there is a significant increase in counts in the RHESSI instrument at the time of lightning flashes, indicating that there are weaker TGFs in existence, and found a $\lambda$ consistent with that predicted by *Østgaard et al.* [2012].

In Chapter 2 we will present the theory that is needed to understand the topic of this thesis. Chapter 3 will outline the work done in the field since 1994 and also explain some of the motivation behind this thesis. Chapter 4 will outline the method we have used to get our results, which are presented in Chapter 5. Chapter 6 will contain the discussion of said results and Chapter 7 will be a short summary of our finding. Chapter 8 contains some suggestions for future work and improvements.

# Chapter 2

# Theory

In this chapter we will present the theory and background that is needed to understand the topic of this master thesis.

## 2.1 Particle Interactions in Electric Fields

### 2.1.1 Runaway Electrons

The runaway electron mechanism is a process by which electrons in strong electric fields gain large amounts of energy and are able to "runaway", and was first proposed by *Wilson* [1924].

This happens in electric fields strong enough so that the energy gained due to the electric field is larger than the energy lost due to collisions. This is however only partly true, as bremsstrahlung will prevent this acceleration going on indefinitely, and will put a limit on the maximum achievable energy of the electron. Figure 2.1 shows the effective frictional force that an electron experience as a function of it's kinetic energy [*Dwyer et al.*, 2012]. Given an initial energy, the electron will experience a retarding friction force $F_D$. The friction force $F_D$ is the result of electrons colliding with neutral gas atoms and molecules in air. If there is an applied force due to the electric field $F_E$, as can be seen by the dashed horizontal lines, it will try to accelerate

the electrons. The net force of these two determine if the electrons will get accelerated or decelerated.

To produce such a runaway effect, the electric fields must be stronger than the so called break-even field which has the theoretical value of $E_t = 2.2 \times 10^5 V/m \times n$, where $n$ is the density of air in respect to sea level[*Dwyer et al.*, 2012; *Moss et al.*, 2006]. The value $E_t$ is shown in Figure 2.1. *Dwyer* [2003] showed through simulations that the real value is $\sim$ 30% higher than the theoretical value due to elastic scattering of electrons. Balloon experiments inside thunderclouds has measured the maximum electric fields close to the break-even field, indicating that a relationship between the lightning initiation process and runaway electron production is possible [*Marshall et al.*, 1995; *Dwyer et al.*, 2012].

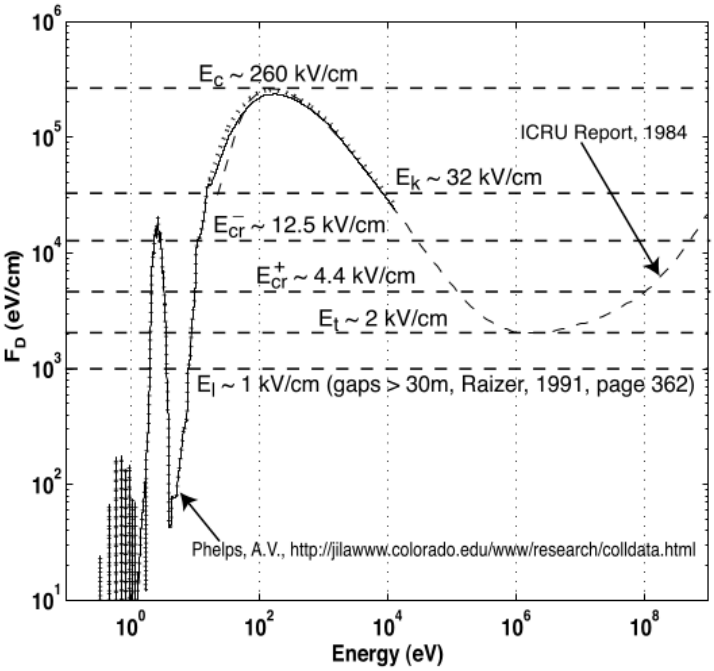


Fig. 2.1: The dynamic friction force of electrons in air at ground pressure is plotted as a function of electron energy. The dashes horizontal lines represents various electric fields. Figure from *Moss et al.* [2006].

The horizontal lines in Figure 2.1 represents various applied electric fields, trying to accelerate the electrons. For an electron to be accelerated it needs to have a certain threshold energy depending on the electric field applied so that the E-field is stronger than the retarding force.

For example, if we have a large region with an electric field of $E_k$ this would trigger a conventional breakdown in air and a subsequent lightning flash. This is seen by the narrow peak in Figure 2.1 at $\epsilon \sim 3$eV. However, it is possible to have this and larger values for the electric field in smaller local areas. In this case, if we apply the electric field of $E_k$ and an electron has the initial energy $\epsilon = 10^4 eV$, it will experience a net accelerating force as the electric field is slightly larger than the friction force. It will then gain energy, moving towards the right of the plot, where the electric force is constant, but the friction force decreases. It will be able to continuously accelerate until the friction force catches up to the electric field again, seen on the far right side of the plot, due to bremsstrahlung.

So to clarify, the friction force and the electric field are competing forces as to accelerate or decelerate the electrons, and whichever is "higher" at a given initial kinetic energy will "win". So for initial kinetic energies higher than the threshold energy, the electric field will have a greater accelerating force than the friction force, and the electrons will continue to accelerate. Electrons with a lower kinetic energy than the threshold energy will decelerate until the electric field and friction force are of equal values (the left of the two intersections). As one can see, electrons beginning from rest will be accelerated, but only to a point where the electric field and friction force intersect. There needs to be an initial electron with a high enough kinetic energy to become runaway *Moss et al.* [2006].

The electrons with an initial kinetic energy above the threshold energy $\epsilon_{th}$ are called "seed" electrons, and may be provided from an external source such as interactions from cosmic rays [*Wilson*, 1924]. As the electric field becomes stronger (as in, the horizontal line moves upwards), the threshold energy for electrons to become runaway electrons decrease, until the electric field becomes larger than the critical electric field value $E_c$, in which all electrons become runaway electrons. This is referred to as a "cold runaway" or a "thermal runaway" [*Gurevich*, 1961; *Moss et al.*, 2006]. This can be seen in Figure 2.1 where $E_C$ is at a larger value then the friction force, providing a net acceleration of all electrons regardless of initial kinetic energy. (However

if the electrons have a higher energy than on the figure, bremsstrahlung will eventually overtake the critical electric field value to prevent the electrons from accelerating indefinitely). This however can only happen locally, as if the electric field reaches the conventional breakdown field $E_k$ on a large scale, a lightning discharge will happen.

### 2.1.2 Relativistic Runaway Electron Avalanches RREA

As we discussed in Section 2.1.1, in strong electric fields, runaway electrons are formed when the accelerating electric field is stronger than the friction forces. Some of these friction forces are due to the elastic Møller scattering with atomic electrons, and in some cases, the initial runaway electron may knock loose an atomic electron. If the atomic electron now has a kinetic energy above the threshold energy $\epsilon_{th}$, it too will become a runaway electron. This process can repeat itself many times, where the accelerated electrons can knock off bound electrons that themselves become accelerated and runaway, which again can knock off more bound electrons. This produces an avalanche of runaway electrons, REA (runaway electron avalanche). If the electrons achieve relativistic velocities, the avalanche is referred to as a relativistic runaway electron avalanche (RREA). The threshold electric field to produce such a RREA was estimated by *Dwyer* [2003] to be $E_t^* = 2.84 \times 10^5 \mathrm{V/m} \times n$, 30% higher than the $E_t$ in Figure 2.1.

### 2.1.3 Avalanche length and time scale

To describe the development of a RREA, we use the avalanche length $\lambda$ (also called growth scale length in some cases), a parameter that describes the rate of growth of the avalanche. $\lambda$ is the length required for the total number of electrons to increase by the natural number $e$. *Dwyer* [2003] used this to produce an Equation of the total number of electrons produced by one avalanche.

$$N_{RREA} = N_0 e^{L/\lambda} \tag{2.1}$$

Where $N_0$ is the initial number of seed electrons at the start of the avalanche,

$L$ is length of the potential difference region, $N_{RREA}$ is the number of electrons at the distance $L$, and $\lambda$ is the avalanche growth scale length. The value of the avalanche length $\lambda$ has been found by Monte Carlo simulations, done by *Dwyer* [2003] seen in Equation 2.2, where $E$ is the electric field, and $E_{th}$ is the threshold electric field for runaway breakdown at 1 atm pressure. Many others have later confirmed this value [*Celestin and Pasko*, 2011; *Inan and Lehtinen*, 2005; *Lehtinen et al.*, 1996; *Coleman and Dwyer*, 2006].

$$\lambda \approx \frac{7.3MeV}{E - E_t} \tag{2.2}$$

We can see that a larger electric field above the electric field threshold will produce a smaller value for $\lambda$. This means that a larger electric field, will increase the electrons produced by the avalanche over a length $L$, seen in Figure 2.2.

### 2.1.4 Relativistic feedback

Through the RREA process, there can be produced up to $\sim 10^{14}$ [*Dwyer*, 2003] runaway electrons assuming only one seed electron. The number of $\lambda$ needed to produce this can vary depending on the local electric field strength, as well as the size of the region. If we assume a local electric field of 2 $\mathrm{MVm}^{-1}$, this corresponds to an avalanche length of $\sim$ 5m, meaning we need about 32 avalanche lengths to reach $10^{14}$ runaway electrons. This corresponds to a region of $\sim$ 160 meters.

However, $10^{14}$ runaway electrons are not enough to explain the number of TGF produced gamma-rays detected at satellite heights. A TGF detected by RHESSI has on average $\sim$ 25 counts [*Grefenstette et al.*, 2009], requiring around $10^{17}$ gamma-rays at the origin of the TGF [*Dwyer and Smith*, 2005]. *Dwyer* [2003] proposed to expand the current mechanism of the RREA to include a so called feedback mechanism. This feedback mechanism included feedback effects from positrons and gamma-rays, explaining the missing numbers of produced energetic electrons. By this mechanism, the avalanches of runaway electrons produce bremsstrahlung X-rays that can either Compton backscatter or pair produce. If the runaway electron produce X-rays through Compton backscattering, these X-rays could travel back to the region where

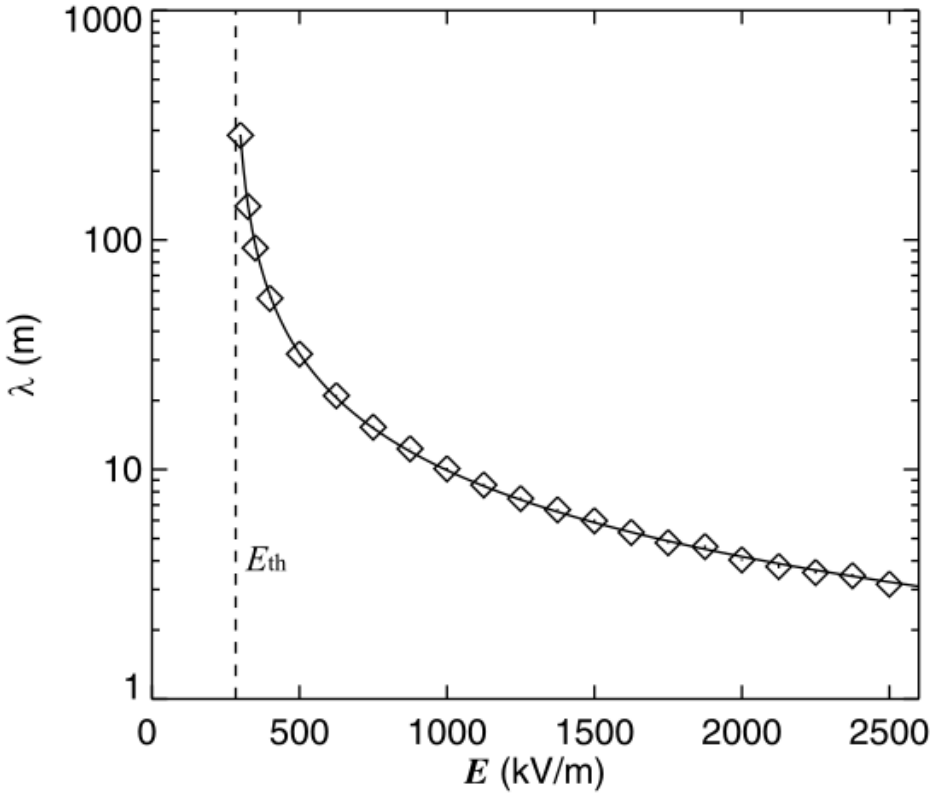


Fig. 2.2: Avalanche length, $\lambda$, as a function of the electric field strength $E$. The data points are calculated by the Monte Carlo simulation and the solid curve is given by Equation 2.2. The vertical dashed line shows the threshold, $E_t$, for runaway breakdown to occur. Adapted from *Dwyer* [2003].

the original seed electron started the avalanche. It could then produce new runaway electrons either through Compton scattering or photoelectric absorption. These new runaway electrons can start a new avalanche, a so called secondary avalanche, if their initial kinetic energy is high enough. On the other hand, the X-rays produced by bremsstrahlung could also pair produce into an electron/positron pair. If this happens the electron will move along the electric field like all other electrons produced by the avalanche, but the positron will be accelerated the opposite way, and can quickly accelerate to tens of MeV [*Babich et al.*, 2005; *Dwyer*, 2003; *Dwyer et al.*, 2012; *Moss et al.*, 2006]. As a result, it can travel to the region of the original avalanche and produce a secondary avalanche by Bhahba scattering with

atomic electrons in air. These types of secondary avalanches can progress, and via bremsstrahlung produce more X-rays and electron/positron pairs, resulting in more feedback and tertiary and higher order avalanches. This way, the total number of runaway electrons is greatly increased due to the possible large number of avalanches possible on a microseconds timescale [*Dwyer*, 2003]. Figure 2.3 shows the result of a simulation of this feedback mechanism.

There is also a competing theory explaining the production of the required number of gamma-rays at satellite altitude. This is based on lightning leaders and streamers themselves being able to produce the required amount of energetic electrons. We mainly concern ourselves with the RREA and feedback mechanism, however the streamer/leader theory will be shortly discussed in Section 2.3.

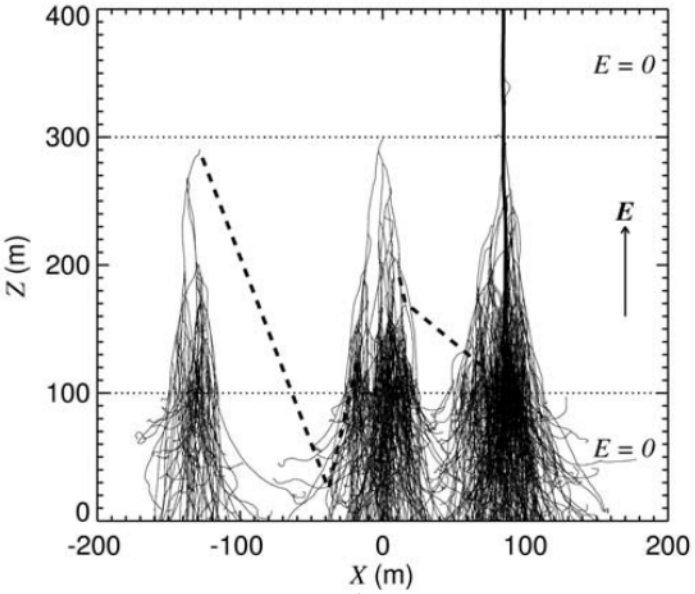


Fig. 2.3: Results of simulations showing the runaway breakdown of air. The dark lines are RREAs and the dashed lines are the X-rays and the dark solid line is a positron (seen a x = 100m and Z $\geq$ 250m). The avalanche is initiated by a 1MeV seed electron injected at the top of the high field region (x = 0, z = 300 m). The horizontal dotted lines represents the boundaries of the electric field volume (E = 100kV/m). One should note that only a small fraction of the total number of runaway electrons, X-rays and positrons are plotted. The avalanches on the left and right illustrate the X-ray feedback and positron feedback mechanisms respectively. Figure and text from *Dwyer* [2003].

## 2.2 Physics of Thunderclouds

Lightning flashes are primarily produced by the type of cloud called cumulonimbus, but not every cumulonimbus produce lightning. Although thunderclouds and thunderstorms are often used as synonyms, a thundercloud is considered to be a lightning producing cumulonimbus and a thunderstorm to be consisting of several thunderclouds [*Rakov and Uman*, 2003]. In this section we will describe how electric fields are produced in thunderclouds, as well as the different types of lightning that occur in thunderclouds. This section will largely be based upon the work of *Rakov and Uman* [2003] and *Cooray* [2008].

### 2.2.1 Charge separation in thunderclouds

There are several proposed electrification mechanisms proposed over the years, however, we will here present two of the more promising ones, namely the *Convection mechanism* and the *Graupel-ice mechanism* they both have in common the following key points [*Rakov and Uman*, 2003]:

- a small-scale process that electrifies individual hydrometeors
- a process that spatially separates these charged hydrometeors by their polarity

Hydrometeors refer to small particles consisting of ice and water droplets. As a result of the separation process, the distances between the charge centres in the cloud can be in the order of kilometres. The hydrometeors are also considered to have a very low mobility, effectively reducing the leakage currents between charge centres, and the cloud is considered a good electrical insulator [*Rakov and Uman*, 2003].

#### Convection Mechanism

In the convection mechanism the electric charges deposited in the clouds are explained due to outside sources, such as fair weather space charge and cosmic rays. According to this mechanism, fair weather space charge are brought in from below, under the cloud, and through updraft the charged packets of

air are brought upwards into the cloud and towards the top. Just above the cloud, negative electric charges are produced by cosmic rays, and attracted towards the boundary of the cloud due to the positive charges deposited here by the fair weather space charge. As the negative charges attach the cloud, they form a so called screening layer of negative charge. An illustration of this can be seen in Figure 2.4.

The negative charge deposited on the top boundary of the cloud carried down the sides of the cloud, towards the base, through processes of cooling and convective circulation. As the negative charge travels down the cloud, it will end up towards the base of the cloud, and will start to produce a positive corona of charge from the surface of the Earth, providing a positive feedback mechanism to the charge accumulation in the cloud. The result of this mechanism is a positive dipole and structured charge centres as seen in Section 2.2.2.

However, the weak point of this proposed mechanism is that is offers no explanation for why the charge regions would be in similar temperature ranges for various thunderstorms. Furthermore it does not explain the role of precipitating particles.

### The Graupel-ice mechanism

On the contrary of the *Convection mechanism*, the *Graupel-ice mechanism* is not dependant on the external sources for electrification. In this mechanism, the electrification occurs due to collisions between various particles inside the cloud.

Graupel is a type of precipitating particle, and precipitating particles are defined as hydrometeors with fall speed of $\geq 0.3ms^{-1}$ [*Rakov and Uman*, 2003]. Particles with a fall speed of $\leq 0.3ms^{-1}$ are considered to be cloud particles. Precipitating particles are generally larger than cloud particles, however there are no defined set of rules of determining the particle by size.

In the Graupel-ice mechanism, the charge separation in the cloud is produced by collisions between Graupel and cloud particles, more specifically ice particles in the presence of water droplets. As the heavier Graupel particles fall downwards through the large mass of ice crystals in the clouds, it will attain charge when colliding with the ice crystal. *Jayaratne and Saunders*

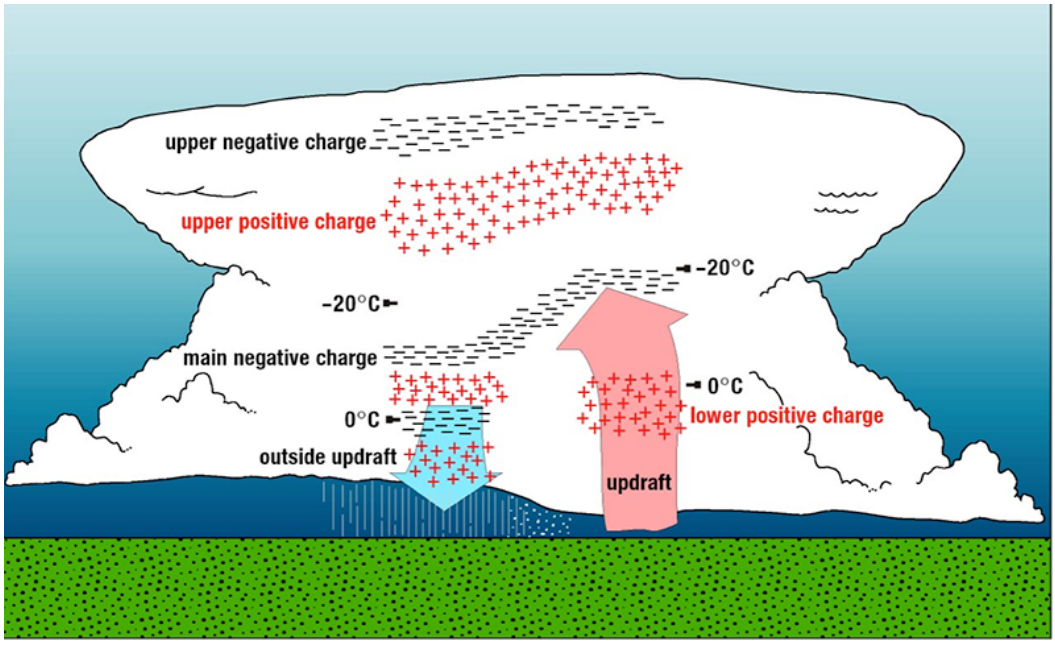


Fig. 2.4: Shows how the convection mechanism create different charge layers in the cloud. It includes a screening layer on top as well as several charge centres. Taken from *Stolzenburg et al.* [1998].

[1983] showed that there is a specific temperature that dictates if the graupel accumulates positive or negative charges, called the reversal temperature $T_R$. This reversal temperature was found to be somewhere between $-10°C$ and $-20°C$. As a result, Graupel in temperature regions below -20 degrees will acquire negative charges, and Graupel in temperature regions above -10 degrees will acquire positive charges. This is illustrated in Figure 2.5

The reversal temperature typically happens at an altitude of 6km and can be used to explain the lower positive charge centre explained later in Section 2.2.2.

In addition to the temperature variable, there are several more factors involved in determining the sign and magnitude of the electric charge separated in these collision. These include, but are not limited to, cloud water content, ice crystal size, relative velocity of the collisions, chemical contaminations and the supercooled droplet size spectrum. It was also shown in *Jayaratne* [1998] that smaller droplets of sizes smaller than $10\mu$m can produce more

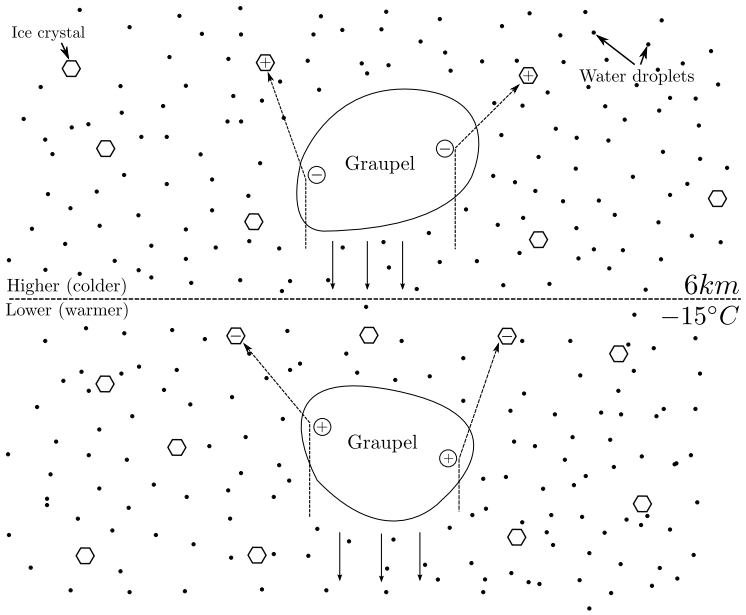


Fig. 2.5: Shows the mechanism for charge accumulation in graupel above and below the reversal temperature. The graupel in the lower/warmer section will gain an overall positive charge from its collisions, and the graupel in the higher/colder section will gain overall negative charge. Figure adapted from *Rakov and Uman* [2003].

than one reversal temperature. In fact restricting the droplet size to less than 4$\mu$m would produce four reversal temperatures, and Jayaratne argued that this could explain the multi-layer cloud charge distributions found in other cases.

### 2.2.2 Charge distribution in Thunderclouds

The distribution and motion of electric charge in thunderclouds are complicated and are subject to continuous change as time progresses, however there are several ways of simplifying such systems in order to understand and model them. Most of the electric charge contained in a thunderstorm resides on the so called hydrometeors, consisting of ice particles and liquid water particles. Some of the electric charge is contained by free ions.

When it comes to modelling such thunderclouds, one often finds that simple models are better than more complicated ones. The model used here, though simplistic, is commonly used to represent the charge distribution in clouds. The model is based on a simple electromagnetic tripole, where the cloud is split into three charge centres stacked on top of each other vertically, as can be seen in Figure 2.6 [*Rakov and Uman*, 2003].

The three charge centres in the simple model consist of a large positive charge on top, often referred to as the main positive or the upper positive. The middle charge centre is usually referred to as the main negative and is considered to be of the same magnitude as the upper positive. The bottom charge, called the lower positive, is however much less in magnitude than the two other. The values given in Figure 2.6 are typical charge values for a thundercloud and give the top charge centres the values of +40C and −40C respectively. The lower positive has a value of +3C [*Rakov and Uman*, 2003] in this model, however this charge may not always be present. The two main charges form a positive dipole (as the dipole moment is upward directed) above a perfectly conducting ground. To calculate the electric field produced by the simple model we can use the method of images.

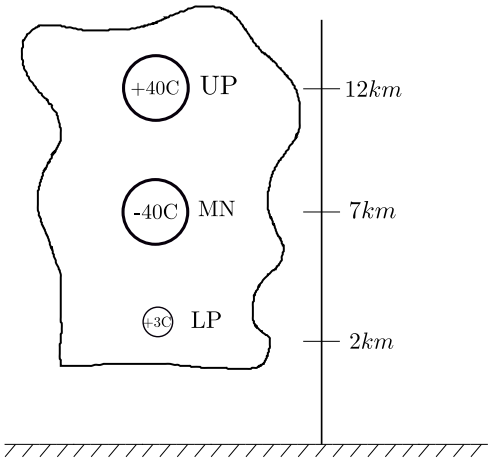


Fig. 2.6: Shows the charge distribution of a cloud after the simple tripole model. At the top is the Upper Positive charge centre (UP), the middle has the Main Negative (MN) and the Lower Positive (LP) at the bottom. Typical charges for the charge centres as well as typical heights for the charge centres are indicated. Figure adapted from *Rakov and Uman* [2003].

### Method of Images

The method of images is a method of calculating electric fields and potentials that arise from working with infinite conducting planes. Looking at Figure 2.6 we see three charges above the Earth's surface (which we consider as an infinite conducting plane).

Using the method of images, one can replace the infinite conducting plane with another mirrored charge. This is allowed as long as we satisfy the boundary conditions associated with the problem [*Griffiths and Inglefield*, 2005]. In this case we have that:

$V = 0$ when $z = 0$

$V \to 0$ for $x + y + z \gg d$ [*Griffiths and Inglefield*, 2005]

Where $V$ is the voltage, and $d$ is the distance between the point charge and the conducting plane, as seen in Figure 2.7.

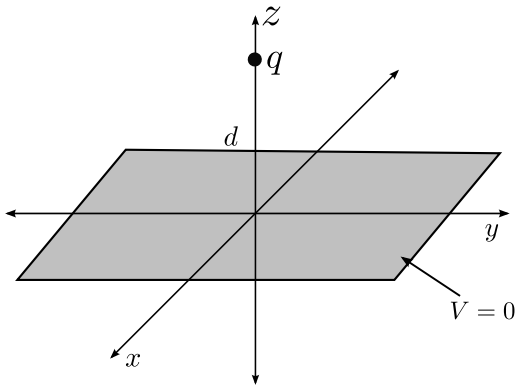


Fig. 2.7: Shows a charge located over an infinite conducting plane. Adapted from *Griffiths and Inglefield* [2005]

The goal of the method of images is to be able to add together the electric fields of each of the charge centre and find the total field produced by the sum of the charge centres. Figure 2.8 shows the computed electric fields based on the method of images. The figure shows the Electric field component of each of the charge centres, as well as the total electric field the system produces.

Looking at Figure 2.8, we can see that although the main positive and main negative charge centres are of the same value, due to the main negative charge centre being at a lower altitude, it dominates over the positive one at distances of 3 to 10km. At distances $-3$ to 3km we see that the lower positive charge centre again dominates, even though it's the smaller of the three, due to it's lower position.

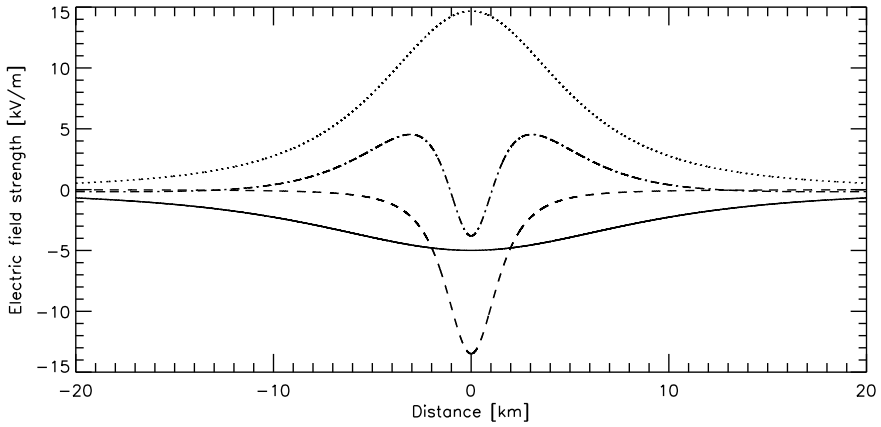


Fig. 2.8: Shows the normal component of the electric field given by the simplified charge model seen in Figure 2.6. The solid line is the resulting Electric field from the Main Positive charge centre at $12km$, $40C$. The dotted line represents the main negative charge centre at a height of $7km$ and a charge of $-40C$. The dashed line represents the lower positive charge centre with a height of $2km$ and a charge of $3C$. The dot dashed line shows the total normal component of the combined electric field found by using the method of images. Adapted from *Rakov and Uman* [2003].

### 2.2.3 Types of Lightning

When it comes to the classification of lightning we usually distinguish between 2 main types of lightning. The first of these types are Cloud to Ground lightning flashes. As the name indicates, these are flashes that discharge from the cloud into the ground, and are often abbreviated as CG lightning. The other type is air discharges, lightning discharges that happen either between clouds (Inter Cloud lightning), inside clouds (Intra Cloud lightning) or from

a cloud to air. These are abbreviated as IC lightning. Although it is estimated that around 75% of all lightning discharges are of the IC type, these are harder to study [*Boccippio et al.*, 1999].

We should also clarify the difference in terminology when it comes to lightning flashes. A lightning discharge is synonymous with a lightning flash. A lightning strike however, refers to lightning discharges that involve objects (such as rocket-triggered lightning strikes) or the ground (as the case with a CG lightning strike). A lightning stroke refers to a component of the lightning strike [*Rakov and Uman*, 2003]. We will mainly refer to either lightning flashes or lightning discharges in this thesis.

In addition, one distinguishes between positive and negative lightning, and it's important to differentiate between the two. Positive lightning refers to lightning flashes that discharge a positive charge centre in the cloud. A negative lightning discharges the negative charge centre in a cloud. This can be a difficult convention to keep track of when dealing with IC lightning strikes, so we will introduce a different convention.

We define a displacement vector, $z$ as the direction from the cloud to the ground, where going downwards is the positive $z$ direction. We can by this convention give polarities to lightning flashes by the direction the charge moves. A lightning flash transporting negative charge downwards is negative, and transporting negative charge down is the same as transporting positive charge up (as it is really only the negative charges moving). Similarly, transporting negative charge upwards, is the same as transporting positive charge downwards. This way, the polarity of the lightning flash is the same as the charge being moved downwards (with positive $z$) or opposite if the charge is being moved upwards.

### CG lightning

Cloud to ground lightning are again split into four different types:

1. Downward negative lightning
2. Upward negative lightning
3. Downward positive lightning

4. Upward positive lightning

These lightning types can be seen in Figure 2.9. Although there are four different types of CG lightning, the downward negative lightning (as seen in Figure 2.9(a) account for around 90% of all CG lightning. Downward positive lightning (Figure 2.9(c)) accounts for almost 10% of all CG lightning, leaving less than 1% to the upward going lightning types. In fact, upwards travelling lightning flashes are thought to only occur from tall objects or objects on top of mountains [*Rakov and Uman*, 2003].

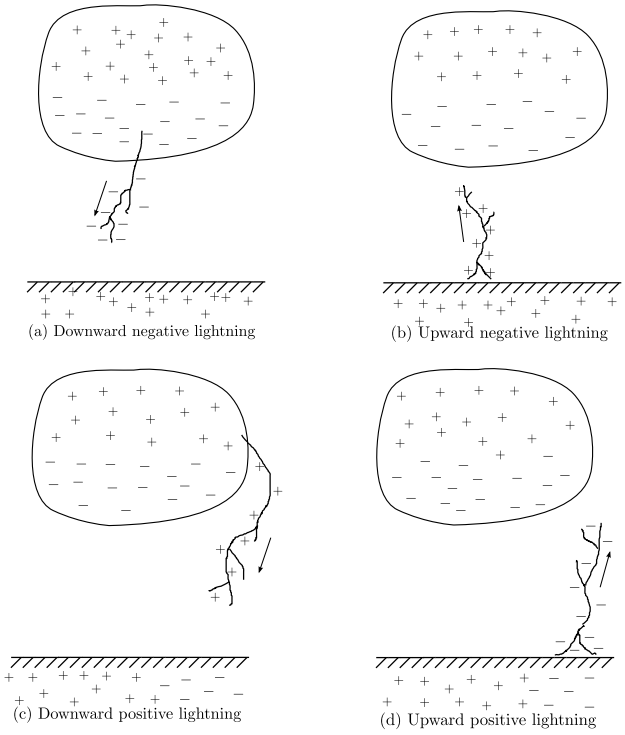


Fig. 2.9: Shows the different types of lightning, and the initial mechanism they have to lower the charge to the ground. The polarities and a rough measure of the charge distribution of the cloud and ground has been shown. Adapted from [*Rakov and Uman*, 2003].

### IC lightning

Although IC lightning are much more common than CG, where around 75% of all lightning flashes are of the IC type [*Boccippio et al.*, 1999], these are much harder to study. Due to this they are less well documented than the CG type.

We mainly distinguish between three separate types of IC lightning. Inter cloud lightning flashes are flashes that occur between different thunderclouds. Intra cloud lightning flashes occur inside a thundercloud and cloud to air discharges occur between a cloud and the air. The exact process of a IC flash will be discussed in Section 2.4.

## 2.3 Streamers and Leaders

The streamers and leaders are related to the initiation of lightning discharges, and the mechanisms of the discharge process. They are important processes to understand how lightning are able to discharge through air. Rakov and Uman defines a leader as "Any self-propagating electrical discharge creating channel with electrical conductivity of the order $10^4$ $\mathrm{Sm}^{-1}$" [*Rakov and Uman*, 2003]. "Streamers, on the other hand, are characterized by much lower electrical conductivity; the air behind the streamer tip remains essentially an insulator". Simply said, one can imagine the leader as the conducting "tube" connecting the cloud to the ground (in a CG) where the charge transfer is done. The streamers can be considered as a corona ahead of the leader (although there are many of them and they are smaller), as the leader is propagating downwards (in the case of a downwards CG) and has yet to connect to the ground.

In literature, the difference between leaders and streamers can be difficult to grasp, as some sources use the word streamer to encompass both of these. However in this thesis we will consider them separate, even though they are very much related to each other. The main difference being that the streamers are much smaller and less conductive. Several streamer processes will result in a leader channel, where the conductivity is much larger, and the leader channel is much longer. One can say that streamers are the initial process that makes the leader grow.

### 2.3.1 Streamers

#### Positive Streamer

The formation of streamers is a result of the ambient electric field and the process of thermal avalanches. We distinguish between two different types of streamers, positive streamers, and negative streamers. In a positive streamer, the electron avalanche will propagate towards the positive charge region of the cloud. When the perturbation reaches the positive charge region, the negative electrons will attach to the positive charge region and be absorbed. The streamer channel is of the order of a few centimetres in length and has a radius of a few micrometers. As the avalanche moves towards the negative charge region, it will be followed by a trail of positive charge as well, attracted by the large number of negative charge moving. This will cause a small expansion of the positive charge region into the gap between the cathode and anode, due to the attachment of avalanche electrons. The cathode is of net negative charge (either negative charge region or negatively charged ground) and the anode is either a positive charge region, or a positively charged ground. When another "wave" of runaway electrons arrive they will also attach in a similar manner. As more avalanches hit the growing streamer, the negative charges will be absorbed, and the positive charges will attach closer and closer to the cathode. In this way, the streamer expands towards the cathode (negative charge centre) [*Cooray*, 2008].

#### Negative Streamer

Similar to the positive streamer, the negative streamer starts with the initiation of a thermal breakdown (see Figure 2.1). This means there must be an electric field of around $\sim$ 30kV/cm to initiate this. This is a very high electric field, but only needs to happen locally. As the electron avalanche move towards the positive space charge (or ground) they leave behind positive charges. The positive charges produced by each subsequent avalanche will be attracted towards the negative space charge, and the positive streamer channel will attach to it. The positive ions will be neutralised by negative charges from the negative space charge. This creates a weakly conductive channel between the negative space charge, and the origins of the avalanches, and the electric field of the negative space charge extends into the streamer

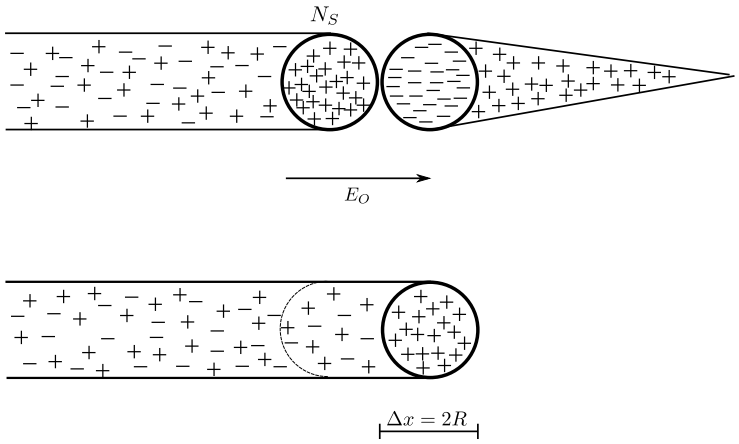


Fig. 2.10: Schematic representation of the propagation of a positive streamer. Adapted from *Cooray* [2008].

tip. As a result, when a new avalanche starts, the streamer tip will push the new electrons further into the gap, while positive charges left behind will be neutralised by electrons supplied by the negative charge space. The electrons from the negative charge space travel through the weakly conducting channel, and with each avalanche, this channel grows, travelling towards the positive charge space [*Cooray*, 2008].

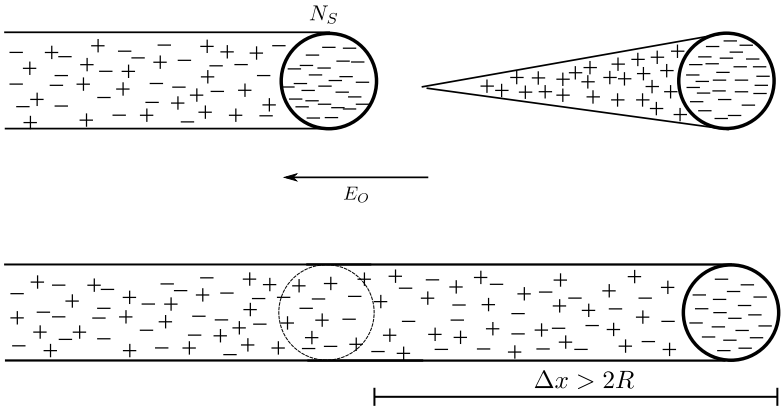


Fig. 2.11: Schematic representation of the propagation of a negative streamer. Adapted from *Cooray* [2008].

Due to these features, the propagation of negative streamers are significantly

harder than that of positive streamers, in fact according to *Moss et al.* [2006] it can be almost a factor 3 difference (see Figure 2.1). Whereas we need a local field of $E_k = 32\text{kVcm}^{-1}$ on the streamer tip, the overall field must be $E_{cr}^{-} \sim 12.5\text{kVcm}^{-1}$ for the negative streamer to propagate and $E_{cr}^{+} \sim\text{kVcm}^{-1}$ for the positive to propagate.

### 2.3.2 Leaders

Some sources refer to leaders as streamers and differentiate between leaders (which they call streamers) and the streamers (which they call the active region of streamers, or the "streamer head"). It is important to not get confused by this.

The main difference between leaders and streamers are the size and conductive differences. Leader channels are very hot and are considered highly conductive with a conductivity of $> 10^4$ Sm whereas the streamer has a relatively low conductivity *Cooray* [2008]. This is due to the leader channel being a weakly ionised "tube" or path for charge to propagate between the charge centres (if connected). This channel consist of a quasi neutral plasma, with an excess of positive charge in the case of the positive leader or excess negative charge for the negative leader.

The leader's propagation progress is being lead by the streamers, as streamers are formed ahead of the leader, and the leader will propagate into the streamer region (or streamer corona), making it a part of the leader. Figure 2.12 shows how a leader propagates in a small scale laboratory setting.

### 2.3.3 Multiplication of energetic electrons

In Section 2.1 we discussed the mechanism for the production of large amounts of energetic electrons, which in turn produce the bremsstrahlung that TGFs consist of. There is however another theory on how these energetic electrons are produced. We will not go into great detail about this, but it should be mentioned.

*Celestin and Pasko* [2011] argues that streamer tips can provide an electric field stronger than $E_c$ (See Figure 2.1). This has the ability to accelerate the

electrons to higher energies without a seed electron from cosmic rays. It is then believed that the seed electrons produced by the streamer tip will initiate RREAs that can again account for the number of photons needed to produce detectable TGFs at satellite altitude. This mechanism also does not include a feedback theory [*Celestin and Pasko*, 2011; *Carlson et al.*, 2009].

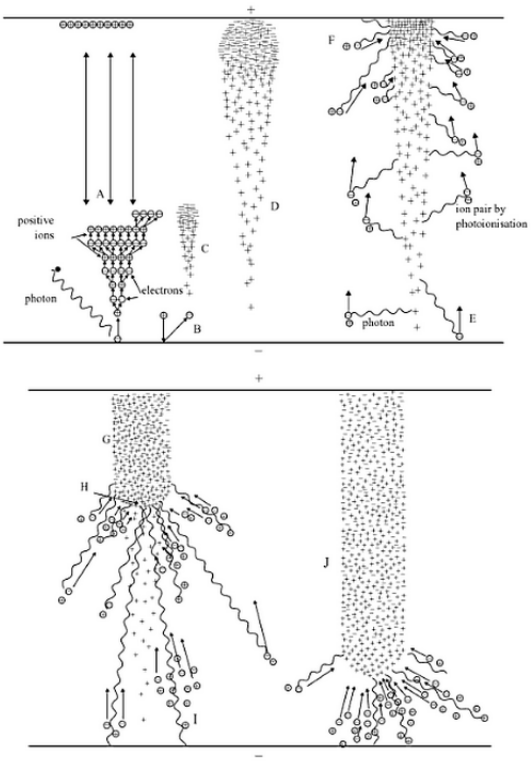


Fig. 2.12: Schematic diagram showing the formation of a positive leader. A: an external photon triggers an avalanche. B: a positive ion strikes the cathode and starts an avalanche C. D: the avalance tip reaches the anode. E: photons originating from the avalanche produce free electrons both from the cathode and in the gas. F: the positive space charge close to the anode increases the electric field and a streamer is just about to be formed. G: plasma of positive ions and electrons forms the streamer channel. H: streamer tip. I: production of free electrons by photons. J: streamer close to the cathode. Figure and text from *Cooray* [2008].

## 2.4 The Lightning Sequence

As the electric charge in cloud systems builds up free electrons experience an increasing electric field between these charge centres. When the electric field becomes sufficient, we experience electric breakdown in air, allowing currents to travel in what is otherwise an electrical insulator. In this section we will describe the processes that allow streamers and leaders to form between the cloud to the air, and how electric charge is discharged.

We will first consider positive and negative cloud to ground lightning, (+CG and -CG) as these comprise essentially all cloud to ground discharges. The other types we will describe are cloud discharges (IC). The reason we will focus on the CG lighting strike is that most lightning location networks are biased towards detecting them rather than the IC, and as we will work with a lightning location network, we should have an understanding on how they work [*Abarca et al.*, 2010]. However, it is currently believed that IC lightning strikes are the culprit behind TGFs observed in space [*Cummer et al.*, 2011; *Connaughton et al.*, 2013; *Østgaard et al.*, 2013], and will be discussed in Section 2.4.3.

### 2.4.1 Negative cloud to ground lightning discharges

These are discharges that originates inside the cloud, and propagates in a general downwards direction. Negative CG transports negative charge to the ground, or one can say the negative charge centre in the cloud gets discharged. Negative CG flashes account for around 90% of all cloud to ground lightning strikes.

Figure 2.13 gives a step by step process on the time evolution of the processes of a CG lightning. We can see that the cloud starts out with cloud charge distribution explained in Figure 2.6. The following step is the initial breakdown (often called preliminary breakdown). There has yet to be a consensus on the mechanism of the preliminary breakdown, however *Rakov and Uman* [2003] suggests it could be a discharge bridging the main negative and the lower positive charge regions, as seen in Figure 2.13. Regardless, this process lasts in the order of a few milliseconds, and sets the conditions for the formation of the stepped leader.

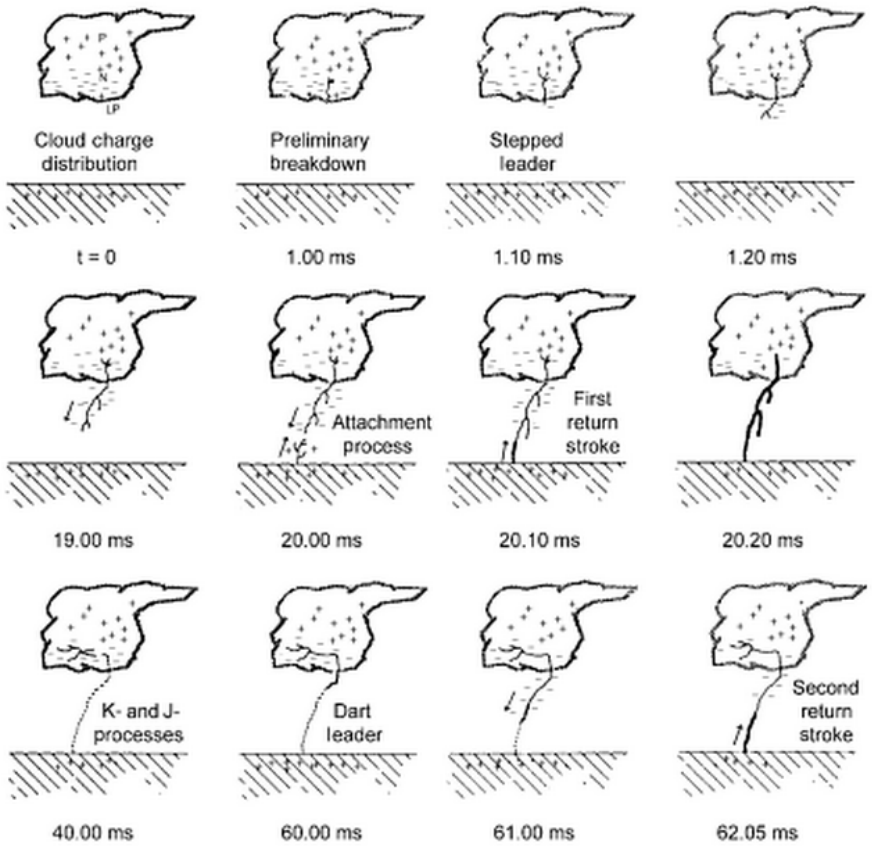


Fig. 2.13: Various processes comprising a negative cloud-to-ground lightning flash. Figure from *Rakov and Uman* [2003].

The stepped leader is the first leader extending from the thundercloud. In the case of negative CG lightning, they are negatively charged plasma channel with a high level of conductance. The stepped leader gets its name for the way it propagates downwards, in discrete steps, with an average speed of $2 \times 10^5$ ms$^{-1}$. Each step is around 1$\mu$s in duration and in the order of tens of meters in length, and a 20 to 50$\mu$s time interval between steps. The stepped leader forms the initial conducting path as it propagates forward, as well as producing branches in different directions.

As the negative stepped leader propagates downwards and approaches the ground, the electric field at the ground increases until there is a breakdown, and an upward positive leader is formed. This is the first stage of the attach-

ment process, and can be seen in Figure 2.13 on the step labelled "attachment process". This attachment process ends when the downwards negative stepped leader meets the positive upwards leader and they come into contact. The point of contact usually happens a few tens of meters above ground, depending on if it was initiated by some elevated object nearby. As contact is established, we now have a highly conducting plasma channel bridging the negative charge centre to the ground, and it initiates the return stroke. The return stroke serves to neutralise the negative charge in the leader by transporting it to the ground. The return stroke is the optically brightest part of the lightning, and the average speed of the electrons in the channel is around one half to one third of the speed of light. Observing the return stroke in slow motion will make it seem that the increased brightness of the channel is moving upwards. This is due to the fact that charge on the lower end of the leader channel are first accelerated as the electrons further up don not "know" that their leader channel has connected [*Rakov and Uman*, 2003].

The return stroke lowers several coulombs of charge deposited in the leader channel, including the charge deposited in the various branches of the leader. Due to the large amount of charged particles rapidly accelerating down the leader channel, the temperature of the leader channel increases to a peak temperature of around 30 000K, and increases the channel pressure to about 10 atm, expanding the channel rapidly. This expansion causes an outward propagating shock wave that is the source of the thunder we hear [*Rakov and Uman*, 2003].

After the return stroke one of two things may happen. Either no more flashes appear, and the lightning is called a single-stroke flash. However, most of the times, the are several more flashes appearing. The subsequent leaders are called dart leaders, as they are able to move faster than the stepped leader, and with a dart leader there is a lot less branching. This can be explained that they are able to follow the original pathway created by the initial stepped leader and return stroke. The dart leaders progress at a speed of around $10^7$ $\mathrm{ms}^{-1}$ and while they generally ignore the previous branches made by the stepped leader, they can break out of the initial channel path and create their own path. In this case they will act like a stepped leader and are in some cases referred to as a dart stepped leader [*Rakov and Uman*, 2003].

As the dart leader approaches the ground an attachment process similar to that with the stepped leader takes place. The upward connecting leader attaches a few meters above ground and the channel discharges with the second return stroke. Any subsequent stroke happens the same way as the second return stroke. The propagation speed of the second return stroke is similar to the first return stroke, though the speed variation along the channel experiences less sudden drops, probably due to the lack of branching of the dart leaders [*Rakov and Uman*, 2003].

After the subsequent return strokes, there is often a continuing current of up to ∼100 ms, considered long continuing currents if they last over 40 ms. The source of the continuing currents are the cloud charges contrary to the charge in the leader channel that is responsible for the lightning flashes.

There might be several subsequent strokes after the return stroke, and some of these might be associated with continuing currents. The time interval between successive return strokes in a flash is on the order of $\sim$ 50ms [*Rakov and Uman*, 2003].

### 2.4.2 Positive Cloud to ground lightning

The positive cloud to ground lightning account for the other 10% of cloud to ground lightning (As positive and negative ground to cloud lightning account for less than 1% of CG lightning). As we have already outlined how negative cloud to ground lightning works, we will now look more at the differences between negative and positive CG lightning.

The +CG lightning flashes are flashes where the positive charge centre in the cloud is neutralised. This means that there must be a supply of electrons from the ground up into the cloud. They are usually comprised of a single stroke contrary to -CG lightning where 80 % contain two or more strokes. Instead they are usually followed by a continuing current lasting for $\sim 10 - 100$ms, where these can reach over 10 kA.

The leaders in +CG lightning also do not behave the same way as in -CG lightning. In +CG lightning the leaders are able to move in a continuous fashion according to time-resolved images, whereas negative leaders are always optically stepped when moving in virgin air [*Rakov and Uman*, 2003].

### 2.4.3 Cloud Discharges

When talking about cloud discharges, we denote 3 different types. The first type is Intra Cloud discharges, these are discharges that occur inside of the thunderstorm. Inter Cloud discharges occur between two thunderclouds, and air discharges are those occurring between a thundercloud and air. These are often all abbreviated under the common term IC flash.

It is estimated that IC discharges account for $\sim$ 75 % of all lightning discharges, though they are far less studied than CG discharges due to the difficulty in acquiring photographic records, as well as the difficulties in measuring the currents and charge transfers happening [*Boccippio et al.*, 1999; *Rakov and Uman*, 2003; *Cooray*, 2008].

The cloud discharges can be considered to be composed of an early stage and a late stage

Intra Cloud Lightning, usually occur between the main negative and and upper positive charge centre (see Figure 2.6). The flash will start with a movement of negative charges from the negative charge centre upwards towardst the positive charge centre, seen in Figure 2.14a and 2.14b. This is indicative of a positive IC lightning, as the positive charge centre is the one being discharged. It can also be explained by the alternative method we introduced, where it starts from the negative charge centre but goes upwards, swapping the polarity and making it a negative IC [*Cooray*, 2008].

This conductive channel (called leader, see Section 2.3) can be up to several kilometres in length and develops at a speed of around $\sim 1.5\times10^5$ ms$^{-1}$.

After the vertical development of this leader channel it extends horizontally inside the positive charge region, seen in Figure 2.14c and 2.14d. In 2.14e and 2.14f, the vertical leader channel loses it's conductivity and the and the upper level channels are cut off from the lower level channels [*Cooray*, 2008].

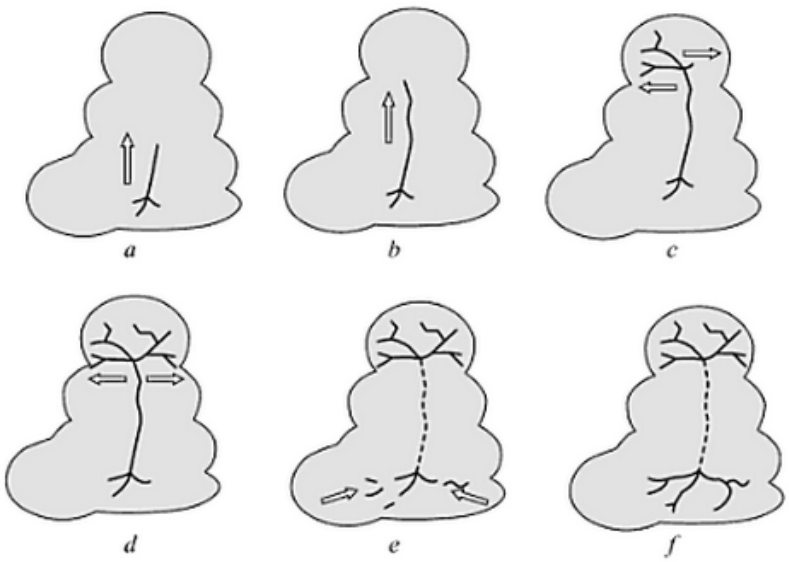


Fig. 2.14: Mechanism of a cloud flash. The cloud flash commences with a movement of negative discharges from the negative charge centre towards the positive one in a more or less vertical direction. This is the initial stage (a and b). This stage is followed by an active stage in which horizontal extension of the upper level channels takes place while charge is being transported from the lower level to the upper level along the vertical channel (c and d). In the latter part of this active stage significant extensions of the lower level channels take place but the extensions take place retrogressively (e). In the final stage the conductivity of the vertical channel decreases and the upper level channels will be cut off from the low level channels (f). The arrows indicate the general direction of the discharge development. Figure and text from *Cooray* [2008].

## 2.5 Terrestrial Gamma-ray Flashes

Terrestrial Gamma-ray Flashes are large bursts of gamma-rays detected during certain lightning discharges. Terrestrial gamma-ray flashes are the most energetic natural phenomenon on the Earth, with energy ranges up to tens of MeV [*Marisaldi et al.*, 2010]. They consist of short bursts of photons of around $\sim$ 0.3ms [*Briggs et al.*, 2013] where $10^{17}$ to $10^{20}$ energetic photons are produced *Dwyer and Smith* [2005]. We know that the energies of these photons can be in the order of tens of MeV, and have been detected at as much as 40 MeV [*Marisaldi et al.*, 2010]. However a frequent problem is that the large number of photons can saturate the instrument. This happens when photons hit the detector right after each other, a so called pile-up, where the detector cannot differentiate if it was hit by one or several gamma-rays.

There are currently two competing production theories of TGFs. One of them is based on a large ambient field that initiates a RREA with feedback from a seed electron (often thought to be a cosmic ray)(See Section 2.1). The other theory considers high local field in the streamer and leader, where a seed electron is produced by the streamer and the electric field of the leader manage to produce a RREA effect (see Section 2.3). Both of these have a large production of electrons, which will produce the energetic gamma-rays through bremsstrahlung.

A lot of the processes that produce TGFs still remain a puzzle, however we know that they are related to lightning discharges, specifically, they are related to positive intra cloud lightning [*Stanley et al.*, 2006; *Cummer et al.*, 2011; *Connaughton et al.*, 2013; *Østgaard et al.*, 2013]. This process brings electrons upwards, which as a result produces bremsstrahlung upwards into the atmosphere. They have been found to happen of the beginning of IC lightning, just after the initiation [*Dwyer et al.*, 2012]. It is currently believed that the production altitude of TGFs is at around 10-20km [*Stanley et al.*, 2006; *Shao et al.*, 2010; *Dwyer and Smith*, 2005].

As the first detection of a TGF was published in 1994, the search of TGFs is still a relatively young science field and there are still a lot of unknowns. This is partly due to the difficulties with direct measurements from thunderclouds, the difficulty in detecting IC lightning, as well as the limitations posed on satellites that are only recently being specifically designed to detect TGFs.

As the runaway electrons produce secondary electrons and these travel in the magnetic field, they produce a current that again produce a radiowaves in the Very Long Frequency (VLF)spectrum. This means that through VLF detection we can find TGF producing lightning flashes [*Cummer et al.*, 2011; *Østgaard et al.*, 2013; *Connaughton et al.*, 2013].

## 2.6 Lightning Detection by VLF

When one gets more than a few hundreds of kilometres away, one can no longer rely on the electric field measurements of thunderclouds to determine the location of a lightning flash. During a lightning flash, the electric and magnetic field involved produce radio waves in the Very Long Frequency band (VLF) at $3 - 30$kHz. These radio waves can be used to triangulate the origin of the source and determine the location of the lightning flash.

### 2.6.1 The Ionosphere

To understand how the VLF waves can propagate several thousands of kilometres, we need to understand how Earth's wave guide works. It was suggested as early as 1902 that there had to be a conducting layer in the atmosphere to explain the observed reflection of radio waves. The existence of the ionosphere was first confirmed by *Appleton and Barnett* [1925]. The ionosphere has its name due to the amount of ionised particles in it, giving it electrically conductive properties. The ionosphere spans a height of around 85km to around 600km and encompasses the thermosphere as well as parts of the exosphere, and have various electron densities depending on the height and the night & day cycle.

The interesting thing about the ionosphere is its behaviour as a waveguide. A waveguide is usually a structure that can guide either sound waves or electromagnetic waves. In the case of the Ionosphere, it is able to guide radiowaves between the ground and the top layer of the ionosphere. This is due to the Earth's surface being ground potential, and the ionosphere being a conductive plane (or technically a sphere) As a result, the radiowaves can travel in this area between the ground and the ionosphere where it will be reflected at the boundaries, shown in Figure 2.15

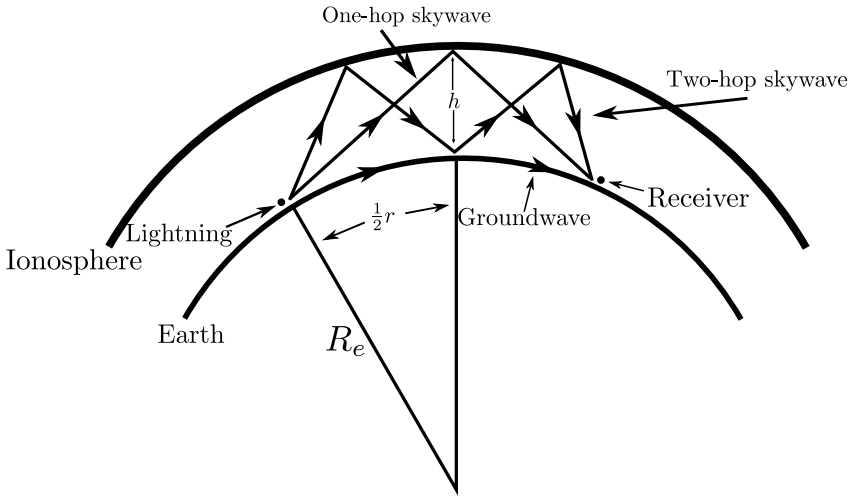


Fig. 2.15: Shows how radiowaves are reflected from the ionosphere as it travels from the lightning towards the detector. Different hop waves will arrive at the receiver at different times. Adapted from *Rakov and Uman* [2003].

### 2.6.2 Sferics

Atmospherics, often called sferics, are electromagnetic waves of the very low frequency band, produced by lightning. Specifically, they are produced by the currents involved in a lightning flash. It has also been found that TGFs themselves can produce sferics due to the number of electrons moving in a RREA *Connaughton et al.* [2013]. Their range is usually in the $3 - 30kHz$ range, and due to the waveguide nature of the ionosphere as discussed in Section 2.6.1, the radiowaves can be detected several thousands of kilometres away.

As the sferic moves some of its energy will be lost through the interaction with the ionosphere, dependant on the frequency of the wave. The reflection of the sferics by the ionosphere is a process that can happen several times, resulting in the sferics "bouncing" between the ground and the ionosphere. This creates a time shift, dependant on the order of "hops" the skywave performs. A one-hop skywave is a sferic that reflects one time from the ionosphere, as seen in Figure 2.15. The same figure shows how a two-hop skywave will travel, as well as the groundwave.

Due to this, the groundwave will be the first sferic to arrive at the receiver, followed by the one-hop skywave, and then any resulting multi-hop skywaves according to the amount of "hop" they have.

## 2.7 Lightning Location

Whenever there is a lightning flash, it produces electromagnetic radiation in the Very Low Frequency range (VLF) at around 3-30kHz. There are two types of detectors involved with measuring these radiowaves. The first class uses magnetic direction finding from each receiving station, and the second class uses the difference in the times of arrival of the lightning radio impulse ("sferic") at each independent pair of receiving stations [*Dowden et al.*, 2002]. This thesis will work with the second of these two classes, as it is what the World Wide Lightning Location Network (WWLLN) is based upon.

### 2.7.1 Systems using timing only

For systems using only the Time Of Arrival (TOA) of the radiowaves, they use the leading edge of the radiowave pulse at each station, which lies in the medium frequency band of $0.3 - 3$ MHz. In this case, they want to avoid the skywaves (see Figure 2.15) and therefore only use the first few milliseconds of the lightning pulse (as this will arrive slightly before the skywave). The lightning pulse is dominated by the return stroke in a CG lightning discharge (however one can also detect IC flashes by this method), and this methods allows a location accuracy to within a few hundred meters.

However the drawbacks of this method is the need for a tight network of detectors with a separation of $\sim$100km as the technique is dependant on the ground wave propagation which has a high rate of attenuation at this frequency, as well distortion of the curvature of the Earth.

The US national lightning detection network uses this detection method and $\sim$100 ground stations have been deployed to cover the US mainland. This is an area of $\sim 10^7$ km$^2$ giving a ground station density of $\sim$10 Mm$^{-2}$. This high density deployment of stations is however not feasible over large areas of low populations or over oceans [*Dowden et al.*, 2002].

### 2.7.2 Time of Group Arrival

A subsection of the TOA systems uses the Very Long Frequency band (VLF) instead of the Medium Frequency band (MF) due to the high power spectral density of lightning. The power spectral density function is a measure of how strong the signal strength is at each frequency at the receiving station. The VLF band has the strongest signal compared to background when dealing with lightning strikes, and is therefore the band being used by lightning networks.

Using the VLF band, one can detect and measure the signals at ranges of several thousands of kilometres, as the radiowaves propagate through the Earth-Ionosphere wave guide. As the detected signal is the resultant of the initial ground wave, and several orders of skywaves, the detected signal is a wave train lasting several milliseconds or more. The amplitude of the wave train, or sferic, rises slowly from the background noise, resulting in no sharply defined time of arrival. To get adequate accuracy of a meaningful time of arrival of the sferic at each pair of receiver sites, the whole VLF wave train is used. This is done by measuring the rate of change of the sferic phase with respect to frequency at the trigger time to find the time of group arrival (TOGA) at each receiver site [*Dowden et al.*, 2002].

To use this method of radio location, where timing only is used with no direction finding, three independent pairs of detectors are needed to determine the location unambiguously. For each detector pair, one needs to find the difference in the time of arrival of the wave train between them. Specifically, one finds the time of group arrival for each of the detectors, and the difference between them to determine the Arrival Time Difference (ATD) for that specific pair of detectors.

Although the time of arrival for wave trains in the VLF band is not well defined, the sferic can be detected when the amplitude of the wide band signal rises from the background noise. *Dowden et al.* [2002] found it to be more effective to use the rate of change of the amplitude as a detection criterion.

One of the advantages of using the TOGA is that there is no need to send the collected data to a central processing station, and instead the lightning locations can be determined differences in the TOGA times [*Rodger and*

*Brundell*, 2004]. The location is then found using the so called Neider-Mead optimization method to work its way back to the original point of the lightning. A schematic of this can be seen in Figure 2.16 which shows the times that different stations detect the TOGA wave train.

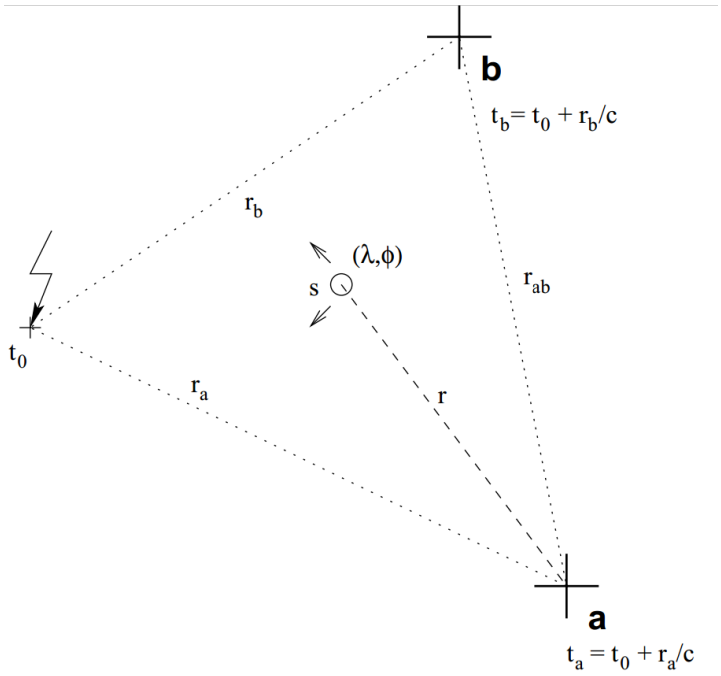


Fig. 2.16: A lightning flash on the surface of the Earth. Stations a and b measure the time of group arrival (TOGA) of the electromagnetic radiation from the discharge. The location algorithm attempts to find an optimal position ($\lambda$,$\phi$ ) for the discharge based on the TOGA measurements. Figure taken from *Rodger et al.* [2009].

# Chapter 3

# Observations

## 3.1 First observations with BATSE

The first TGF was detected in April 1991 by the Burst and Transient Source Experiment (BATSE) experiment on-board the Compton Gamma-Ray Observatory (CGRO). The observatory was launched April 5th, 1991 to a low earth orbit ($\sim$ 450km altitude) with an inclination of 28.5°[*Fishman et al.*, 1994]. Its planned de-orbit happened in June 2000, providing slightly more than 9 years of data. BATSE consisted of 8 sets of scintillators, located on the corners of the observatory, facing outwards, as can bee seen in Figure 3.1, representing each side of an octahedral [*Fishman et al.*, 1994]. As the scintillators face outwards from every corner of the spacecraft they are sensitive to x-rays and gamma-rays from the whole sky. This enables the sources to usually be detected by four detectors, and the relative time differences of detected can be used to estimate the direction of the source. Each module consist of a Large Area Detector (LAD) and a Spectroscopy Detector (SD). The LADs were sheets of NaI 1.27cm thick with an effective area of 2025cm$^2$. The SDs were a cylinder of NaI 7.6cm thick and a diameter of 12.7cm [*Dwyer et al.*, 2012]. Although both of the modules registered the TGFs, literature on BATSE only uses data from the LADs. During BATSE's 9 years of operation it detected 78 TGFs.

BATSE was originally designed to detect galactic gamma-ray bursts [*NASA*, a], however in the first two years its operational time it detected 12 events of

an unexplained phenomenon; brief intense flashes of gamma-rays of terrestrial origin [*Fishman et al.*, 1994]. These results were first published in 1994 by *Fishman et al.* [1994] where they suggested that the source of these gamma-rays could be the bremsstrahlung produced by high energetic electrons. They also linked the TGFs to thunderstorm regions, by using satellite imaging over the areas BATSE had passed over, but their link to lightning flashes was at this point unclear.

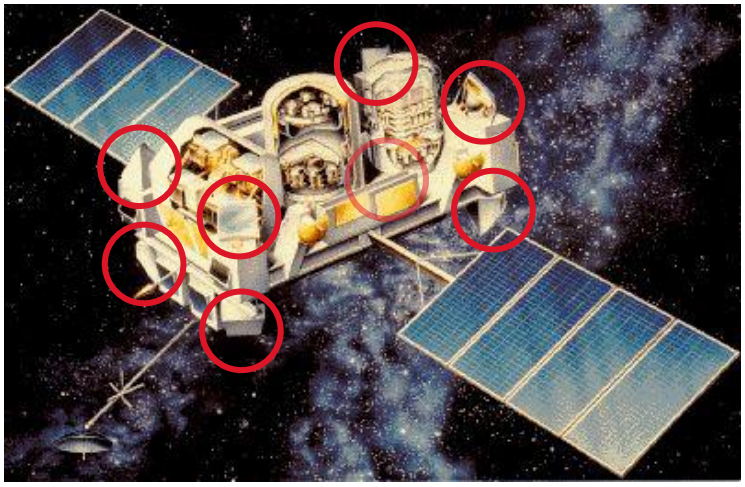

Fig. 3.1: Shows Compton Gamma-Ray Observatory. The individual BATSE instruments are shown in the red circles. The partly transparent circle indicates a BATSE instrument occluded from view. Image adapted from NASA's websites.

The TGF profiles presented by *Fishman et al.* [1994], seen in Figure 3.2, shows that the typical time duration of a TGF is in the order of milliseconds. *Nemiroff* [1997] showed that the duration of TGFs found by BATSE range between $0.67 - 10.71$ ms , far shorter than the Gamma-ray bursts durations it was set to measure (typically a few seconds). The first 12 TGFs shown in *Fishman et al.* [1994] showed time profiles of varying pulse widths and sometimes several pulses (one TGF had five pulses). BATSE was a triggered instrument, meaning it had a built-in algorithm that detected a sharp increase in count rate above background for then to return short intervals of high time resolution data. This means that BATSE's results were given as time tagged events, a format that gave the arrival time for each count in the LADs to $2\mu$s accuracy. The LADs also had a measure of the deposited energy

of the incoming particles, sorting them into one of four channels: $20 - 50$ keV, $50 - 100$ keV, $100 - 300$ keV and $> 300$ keV.

The algorithm that detects an increase in gamma-rays has a trigger window of 64 ms. This means that the incoming gamma-rays must deposit an energy significantly over the background energy over 64 ms, a relatively large time window compared to the short temporal nature of a TGF ( $\sim$ a few ms or less). *Fishman et al.* [1994] suggested that as a result, the long trigger window meant that weaker events would not be seen as significant, and that BATSE was only able to detect the very strong TGFs. *Inan et al.* [1996] also suggested the production altitude of TGFs to be above 30km.

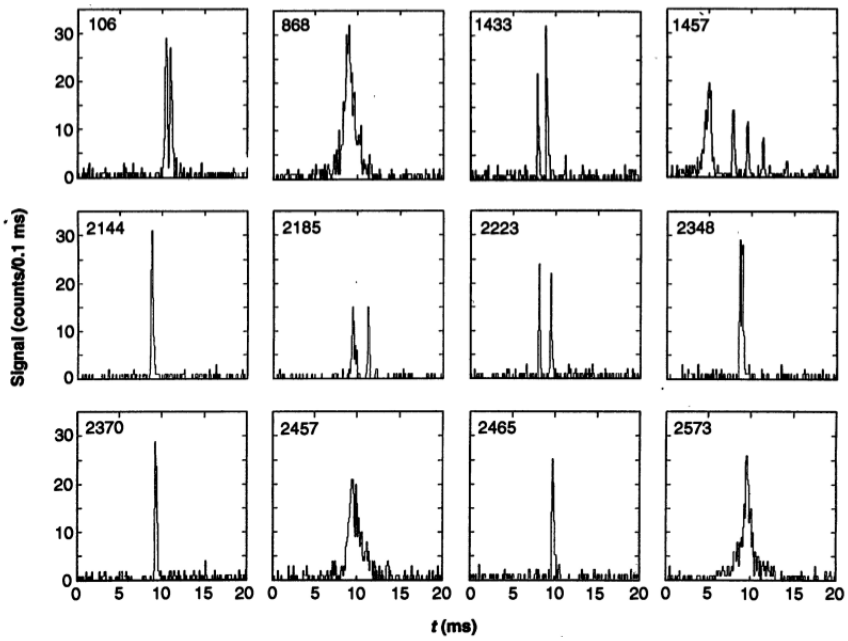


Fig. 3.2: Shows 12 of the TGFs detected by *Fishman et al.* [1994]. The start time is arbitrary and shows the counts of gamma-rays detected split into 0.1ms bins. We can see several of the events having more than one peak. Typical fall and rise times are $\sim$ 0.1 - 2ms. Taken from *Fishman et al.* [1994].

## 3.2 The second wave of TGFs from RHESSI

The Reuven Ramaty High Enery Solar Spectroscopic Imager (RHESSI) was the second source of TGFs after BATSE. RHESSI is part of NASA's small explorer missions and is dedicated to studying solar flares. The satellite carries one instrument; an array of nine high-resolution germanium detectors inside an aluminium cryostat [*Smith et al.*, 2002; *Grefenstette et al.*, 2009; *Dwyer et al.*, 2012]. It was launched on February 5th 2002 and put in a low earth orbit of $\sim$ 600 km with an inclination of 38° and is still operating at the time of writing. The germanium detectors are divided into front and rear segments, where the front segments are used to image solar flares and are not used in TGF detection [*Grefenstette et al.*, 2009], whereas the rear segments view the whole sky.

The RHESSI instrument is much smaller than BATSE, and as a result detects significantly fewer counts in a TGF (a typical RHESSI TGF contains $\sim$ 25 counts) [*Grefenstette et al.*, 2009]. As opposed to BATSE's triggering mechanism, RHESSI continuously collects data that can be investigated on the ground, meaning the data can later be searched with different algorithms. One can then use smaller search windows and find weaker TGFs that would have been able to trigger the BATSE instrument.

RHESSI is also able to detect energies in the range of $\sim$ 3 keV $-$ $\sim$ 17 MeV, and any more than this will be measured in an overflow channel. Due to Compton scattering, one photon may also be able to deposit energy into more than one detector. *Smith et al.* [2005] showed that RHESSI is detecting TGFs with energies up to $\sim$ 20 MeV, much larger than BATSE's highest detectable energy of $\sim$ 300kev. *Dwyer and Smith* [2005] Also found the production altitude to be in the $15-21$km range, lower than 30km suggested by *Inan et al.* [1996].

In the first 183 days of RHESSI's mission, 83 TGFs were detected by *Smith et al.* [2005], more TGFs than had been detected in the entire 9 year operational span of BATSE. The first RHESSI catalogue was presented in by *Grefenstette et al.* [2009] containing 820 TGFs from the period of March 2002 through February 2008. *Gjesteland et al.* [2012] developed a new search algorithm for use on the raw RHESSI data in the period 2004-2006, which more than doubled the detected TGFs for this period. Applying this algorithm on the years 2002-2013 *Gjesteland et al.* [2014] identified $\sim$ 3000 TGFs. It was

also found that the TGFs detected by RHESSI sample contained a larger fraction for single peaked short TGFs, contrary to BATSE's longer multi-peaked TGFs. This was explained by the trigger mechanism on BATSE, requiring a significant signal over 64 ms. *Grefenstette et al.* [2009] on the other hand used a 1ms window in his search algorithm, enabling them to detect fainter TGFs.

It was determined through simultaneous measurements of a solar flare by RHESSI and another satellite (called Swift) that there is a systematic error in RHESSI's internal clock [*Grefenstette et al.*, 2009]. *Grefenstette et al.* [2009] stated that the error is of $\sim 1.8$ms, however this was an estimate and they were not sure if this was a constant error or varying throughout the mission.

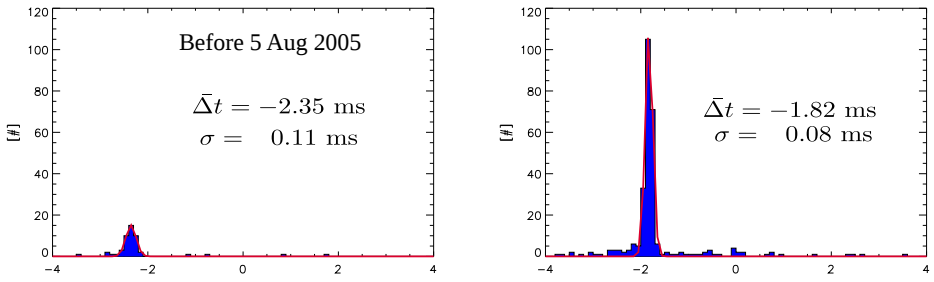


Fig. 3.3: The figure shows the time differences between RHESSI peak time and the time of the WWLLN sferic. Left side shows the error before 5th of August 2005, and right side shows the error after 5th of August 2005. Figure taken from *Gjesteland et al.* [2014].

*Gjesteland et al.* [2014] did an investigation on the systematic error, and found that its value changed on the 5th of August 2005. Before this date the error was of 2.35ms with an uncertainty of 0.11ms. On August 5th, a change was made to the on ground software, reducing the RHESSI clock offset by exactly 0.5ms [*Gjesteland et al.*, 2014]. This can be seen in Figure 3.3, along with a more accurate number for the clock error of $1.82 \pm 0.08$ms

## 3.3 Newest generation with AGILE, Fermi and ADELE

### 3.3.1 AGILE Observations

AGILE (Astrorivelatore Gamma a Immagini LEggaro) is an Italian satellite that was launched April 23, 2007. It was put in a low earth orbit of $\sim 550$ km altitude and a 2.5°inclination. Due to the very small inclination, AGILE spends a lot of time over the tropical regions, places where the lightning density is the highest [*Marisaldi et al.*, 2010; *Tavani et al.*, 2011; *Fuschino et al.*, 2011]. AGILE's instrumentation is sensitive to photons in the range of $0.35 - 100$ MeV, and *Marisaldi et al.* [2010] found TGFs with energies above 40 MeV. Their rate of detection was around 4 TGFs per month, before improving their trigger model March 2009, increasing this to $\sim 8$ TGFs per month.

### 3.3.2 Fermi Observations

The Fermi Gamma-ray Space Telescope (originally Gamma-ray Large Area Space Telescope but renamed in August 2008 after Enrico Fermi) was launched on June 11, 2008 into a low earth orbit of $\sim 580$ km altitude and an inclination of 25.6 °[*Briggs et al.*, 2010]. Similarly to BATSE, its main objective is to study Gamma-ray Bursts (GRB) from celestial bodies and Fermi consists of two instruments; the Large Area Telescope (LAT) and the Gamma-ray Burst Monitor (GBM). The GBM is the only instrument of the two so far to be used to identify TGFs, and it consists of 12 NaI scintillators pointing in different directions and two Bismuth Germanate scintillators [*Briggs et al.*, 2010]. The 12 NaI scintillator detectors has an energy range of $\sim 8$ keV to $\sim 1$ MeV, and the two BGOs have an energy range of $\sim 200$ keV to $\sim 40$ MeV. Similarly to BATSE, Fermi BGM uses an on board trigger algorithm, but with a 16ms accumulation time, much smaller than BATSE's 64ms. As the instrument effective detection area is larger than that of RHESSI's, it is able to provide a much more sensitive data set. In 2010 the Fermi team started downloading data from certain regions with increased TGF production, and later they extended this to downloading all data. This enables them

to do on ground search of the data. This increased the detection ability of Fermi by a factor of $\sim 10$ [*Briggs et al.*, 2013].

### 3.3.3 ADELE Observations

ADELE (Airborne Detector for Energetic Lightning Emission) is an airborne detector made to study TGFs from an altitude comparable to its production altitude [*Dwyer et al.*, 2012]. It managed to detect one TGF from a positive IC flash over Georgia's cost (USA) while flying at an 14km altitude [*Smith et al.*, 2011]. ADELE later passed within 10km of over 1000 lightning discharges detected by ground based lightning location networks without detecting any TGFs. Due to the lack of observations, *Smith et al.* [2011] suggested that TGFs are rare events only associated with 0.1-1% of lightning flashes.

## 3.4 TGFs connection to sferics

The first observations of TGFs by *Fishman et al.* [1994] already speculated on the connection between TGFs and thunderstorms. They used satellite imaging to find a strong connection between the TGFs and storm systems. Several studies has since confirmed the link between TGFs and and thunderstorms, and more specifically, some sort of lightning processes within lightning storms. However, the exact lightning processes involved are still not fully answered.

*Inan et al.* [1996] were the first to study the link between TGFs and lightning produced sferics. By studying two of the BATSE TGFs they found from very low frequency (VLF) recordings that lightning was occurring in the storms seen by the previous satellite images. They also registered a lightning stroke occurring within 1.5 ms of the TGF *Inan et al.* [1996].

This study carried on when the influx of RHESSI TGFs came to light, and *Smith et al.* [2005] showed that the TGFs RHESSI detected in the first 6 months of it's operational fitted well with the world distribution of lightning flashes. *Cummer et al.* [2005] did an analysis on the VLF radio emissions during 26 TGFs registered by RHESSI and found that 13 of them happened

within milliseconds of lightning discharges of positive polarity. The analysis strengthened the view that TGFs and lightning discharges are related, however due to the ∼millisecond uncertainty at the time in the on board RHESSI clock, one could not say if the TGF is produced before, after or simultaneously with the lightning discharge [*Grefenstette et al.*, 2009].

A larger study performed by *Inan et al.* [2006] on RHESSI TGFs supported *Cummer et al.* [2005] in saying that most TGFs are closely associated in time with sferics (However the timing still has an uncertainty due to RHESSI's internal clock)

In 2010, *Cohen et al.* [2010] did an analysis on another 36 RHESSI TGFs used multiple sferic measurements to support the relation between lightning flashes and TGFs. In addition, they used these sferic measurements to geolocate the position of the TGF producing lightning discharge. It was found that the majority of TGFs were detected within a 300km radius of RHESSI's sub-satellite point, though a few were found as far out as 700km.

*Stanley et al.* [2006] did a study on 8 TGFs and managed to link 5 of them to positive IC flashes, agreeing with *Cummer et al.* [2005]. They also determined the altitude of two of them to be of 13.6 and 11.5 km.

*Lu et al.* [2010] found a RHESSI TGF matching the sferics from the North Alabama Lightning Mapping Array (LMA) where they determined that the TGF was produced by a strong positive IC flash. The flash happened between the Main Positive of 8.5km and the Upper Negative of 13km. Their result also indicated that the TGF was produced during the upward leader propagation.

*Shao et al.* [2010] came to the same conclusion as Lu, when using the Los Alamos Sferic Array (LASA), between December 2005 and November 2007. They found that all TGF related lightning events detected by LASA were related to a positive IC flash, even though LASA mostly detects CG flashes [*Shao et al.*, 2010]. They determined that the height of the TGF related lightning flashes to be in the area of $10.5 - 14.1$km.

As Fermi became operational in 2008, *Briggs et al.* [2010] used the much more accurate Fermi clock to investigate the temporal relationship between TGFs and lightning. *Connaughton et al.* [2010] used the WWLLN (World Wide Lightning Location Network) lightning times and the TGF peak times to compare the precise times of TGFs and lightning. 15 of the TGFs were

associated with WWLLN detections and 13 of these were found to have lightning TGF peak times within a 40 $\mu$s window [*Dwyer et al.*, 2012]. This shows a strong degree of simultaneity of TGFs and the process that creates the VLF radio waves detected by WWLLN.

*Cummer et al.* [2011] suggested that maybe the TGFs themselves are the source of detectable sferics by linking the magnetic field data signal to rate of photon count-rate in two TGFs. This can be explained by the runaway electrons moving upwards creating a current, which again creates the sferic. *Connaughton et al.* [2013] suggested the same thing and also found that shorter TGFs were more likely to produce a detectable VLF signal than longer ones. *Østgaard et al.* [2013] also supported that the TGFs themselves could be the source of a VLF signal, when investigating a TGF event happened inside the FOV of both RHESSI and the Lightning Imaging Sensor (LIS) onboard the Tropical Rainfall Measuring Mission (TRMM). VLFs from the event were detected by both WWLLN and sensors from Duke University.

## 3.5 How common are TGFs?

At this point we have viewed some of the development in the TGF area since they were first detected in 1991. However one question that researchers have been trying to answer is; "How common are they?", and this is also the basis for this thesis. In the start they were considered rare events, but as time went by and better, more specific instruments came to light, as well as better search algorithms, more and more TGFs have been found.

In *Smith et al.* [2005] suggested, based on the current evidence, an occurrence rate of $\sim 50$ per day using data from RHESSI. They also pointed out that this would strongly depend on the beaming factor of photons, and depending on this there could be up to $\sim 5000$ per day.

*Carlson et al.* [2009], also using RHESSI, determined that one needed at least more than 500 TGFs per day to account for the number of TGFs detected up to this point. In 2011 *Carlson et al.* [2011]. again revisited this number and estimated a global occurrence of 1400 TGFs per day. They also pointed out that estimates of global frequency would be heavily dependant on the

beaming factor of TGFs. The beaming factor indicates how spread out the beam of photons are, as wider beams will be detectable by satellites with foot-points further from the origin of the TGF. *Briggs et al.* [2013], using Fermi, determined a global production rate of around $\sim$ 1100 TGFs per day, and *Tierney et al.* [2013](Also using Fermi) determined it to be $\sim$ 1200 TGFs per day between a latitude of $\pm$ 25.6°.

These estimations on the global production rate are all based on how many TGFs a satellite manages to detect (as a satellite can only detect TGFs in a given FOV) and extrapolating these results for the entire globe. This means that all estimates are limited by the detection efficiencies of the instruments and the trigger algorithms associated with them. For a signal to be determined to be a TGF, there needs to be a given number of gamma-rays above a certain threshold. If a TGF is so faint that it only deposits 1-5 photons in the detector, this will not be registered as a TGF, because it will be indistinguishable from the background. There is a certain grey area where we cannot tell if a signal is just random noise or a TGF, or even a TGF that just blends in with the background.

*Østgaard et al.* [2012] did another estimate of the global occurrence of TGF by fitting a power law to the current amount of detected TGFs to estimate the number of faint TGFs undetectable by current instruments and search algorithms.

They suggested that the global production rate of 50000 TGFs per day, quite higher than previously suggested, if the TGF distribution has a cut-off at around $\sim$ 1/100 of RHESSI's detection threshold. However if the TGF distribution has a roll-off below $\sim$ 1/3 of the detection threshold they claimed that one cannot rule out that all lightning produce TGFs.

## 3.6 The Fluence Distribution of TGFs

*Østgaard et al.* [2012] made an effort to determine the true fluence distribution of TGFs, through a power function of the form seen in Equation 3.1, where $A_0$ is a scaling factor and $\lambda$ is the exponent of the curve to be determined. Two values for $\lambda$ can be seen in Figure 3.4 where the RHESSI and

Fermi have different values for $\lambda$.

$$\frac{dN}{dn} = A_0 n^{-\lambda} \tag{3.1}$$

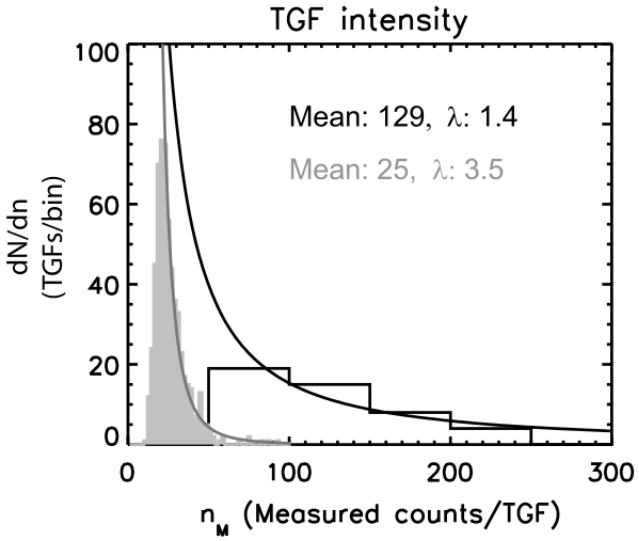


Fig. 3.4: The fluence distributions of TGFs measured by RHESSI (grey histogram) and Fermi (black histogram). Power functions are fitted to both distributions. The average values for Fermi are for TGF pulses, defined as counts in the central 50% of duration. Figure from *Østgaard et al.* [2012].

*Østgaard et al.* [2012] argues that the reason RHESSI has a soft fluence distribution (relatively many low fluence TGFs) is due to dead-time losses in the instrument. The reason Fermi has a hard fluence distribution (relatively many high fluence TGFs) is due to its long trigger window of 16ms. They therefore argue that the true fluence distribution at satellite height must be somewhere between these two. By correcting for RHESSI's dead-time problem using a Monte Carlo simulation (seen in Figure 3.5(a)), *Østgaard et al.* [2012] presented the plot seen in Figure 3.5(b)where the fluence distribution is corrected to the true fluence distribution of 591 RHESSI TGFs.

They found that the exponent of the predicted power function of TGFs went from a value of $\lambda = 3.5$ to $\lambda = 2.3$, when accounting for the RHESSI dead-time (in the figure they present $\lambda = 2.6$, but through some modelling they

determined it to be 2.3). They also suggested that there could be a roll-off at the lower end of the fluence distribution with a $\lambda = 1.7$, seen by the red line.

*Tierney et al.* [2013] also made an attempt to estimate the true fluence distribution at satellite heights using Fermi. Similarly to *Østgaard et al.* [2012], in addition to the TGFs seen in Figure 3.4, they also used TGFs indentified with the on ground search to reduce Fermi's bias towards strong TGFs. They also corrected for Fermi's dead-time and pule pile up (a problem where incoming photons hit the detector very close in time, and the detector cannot differentiate between them), to find an estimate of the exponent in a power function. They found that $\lambda = 2.20 \pm 0.13$, in close agreement with *Østgaard et al.* [2012].

*Smith et al.* [2011] on the other hand disagrees with this power law function, with their study using ADELE. During ADELE's flight in 2003, it passed by 1213 lightning flashes in a 10km horizontal distance. Of these ADELE only detected one TGF at over 20 counts. According to a power law function, this means there should be another 20 weaker TGFs that were not detected. *Smith et al.* [2011] argued that this means that TGF's are rarer than what we originally though. They also rule out the possibility of a large population of weak TGFs.

Similarly to *Østgaard et al.* [2012] and *Tierney et al.* [2013], *Marisaldi et al.* [2014] made an investigation of the true fluence distribution of AGILE. By correcting for dead-time in AGILE they found a $\lambda = 2.4$ when they assumed a sharp cut-off in the true fluence distribution. For a roll-off fluence distribution they found that $\lambda_1 = 1.7$ and $\lambda_2 = 2.6$ which agrees well with *Østgaard et al.* [2012]. *Marisaldi et al.* [2014] pointed out that "It is remarkable that results from three different spacecrafts, with different characteristics and dead time models, point toward consistent results."

This brings us to the motivation for this thesis. Our hypothesis is that there are unidentified TGFs that cannot be distinguished from the background, and we will make an attempt to show that there is an increase in gamma-rays incident on RHESSI at the time of a lightning flash. We will do this by superposing the light curves from a large number of lightning discharges, to see if there is a statistical increase in counts at the time of lightning. Further on, we will investigate the distribution of these counts to determine what, if any, power law exponent it follows.

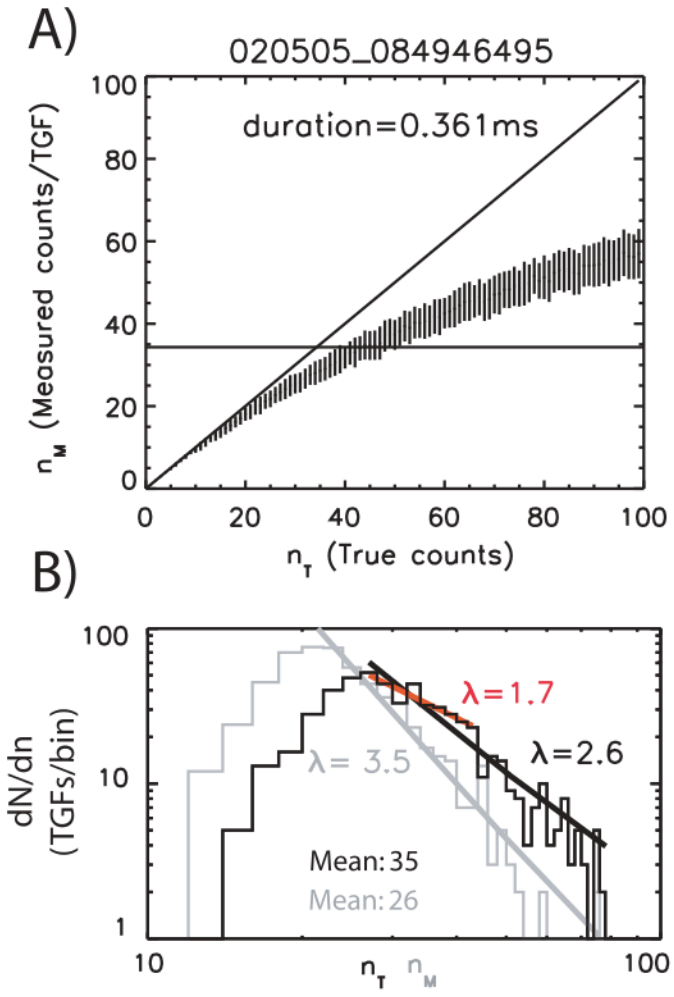


Fig. 3.5: (a) Monte Carlo simulation of the TGF observed May 2, 2005, with a duration of 361 $\mu$s, with increasing true fluence from 0 to 100. Vertical line denotes the measured counts and the true counts can be read out from the intersection between MC values and horizontal line, here 45 $\pm$ 7. The diagonal line indicates that RHESSI has no dead-time losses up to about 15 counts. (b) Grey histogram is the measured fluence distribution of the 591 RHESSi TGFs while black histogram is the true fluence distribution running the MC model on each of the 591 TGFs. Due to background subtraction there are TGFs with less than 19 counts. The black, grey and red lines show the fitted power distributions for the measured ($\lambda = 3.5$) true ($\lambda = 2.6$) and the lower bins of the true ($\lambda = 1.7$). Figure from *Østgaard et al.* [2012].

# Chapter 4

# Method and Data

This section will outline the method, and the programming techniques we have used in this master project. We have two sets of data, namely the WWLLN data, giving the timing and location of lightning throughout the year, and the RHESSI data. As the runaway electrons produce the bremsstrahlung that a TGF consist of, we will find all WWLLN lightning flashes inside RHESSI's FOV and superpose the RHESSI light curves from the time of the flash. First a rough search was performed to find the WWLLN events which happened inside of RHESSI's FOV, saving these as possible candidates, and discarding the rest. Then a more thorough search was performed where the exact location and time of RHESSI was compared to the locations and times of lightning flashes. The light curves centred around the time of lightning was then retrieved (in a $\pm$50ms window).

## 4.1 WWLLN

We will use the World Wide Lightning Location Network (WWLLN) as the source of lightning location data. The network is operated by the University of Washington in Seattle, and they currently have over 70 [*Mallick et al.*, 2014] detectors world wide to detect sferic activity in the VLF band (3-30kHz). To accurately locate a lightning flash, 5 different detectors need to detect the time of group arrival (TOGA, see Section 2.7.2). How accurately the location is determined is dependant of the geographical arrangement

of the surrounding sensors, as a flash that is better enclosed by sensors is more accurately detected as one that is not. As the Earth is spherical, every lightning flash will technically be surrounded by sensors, however this does not necessarily mean that every surrounding station detects the flash. Over the years, the WWLLN network has been able to deploy more receiver stations and increased their detection efficiency, as well as improving the detection software algorithm. According to *Abarca et al.* [2010], the WWLLN detection efficiency for CG and IC flashes was 2.31% in 2006-2007. In 2008-2009 this increased to 6.28%. *Rudlosky and Shea* [2013] reported the global WWLLN detection efficiency to be $\sim$ 10% in 2012, however they pointed out that this detection efficiency is strongly dependant on the geographical position. For example a flash in North America is twice as likely to be detected as a flash in South America. They contribute this to the fact that North America has a much higher density of detectors.

The detection efficiency also depends on how strong the lightning flash is. They estimate their detecting efficiency is around 30% globally for flashes of around 30kA [*Mallick et al.*, 2014; *Rudlosky and Shea*, 2013]. And we have assumed that their altitude is 10km high.

We have access to WWLLN data from 2006 and 2012 with a timing and location uncertainty of 45$\mu$s and 15km respectively [*Østgaard et al.*, 2013].


Fig. 4.1: Shows the WWLLN sensors as of 2013. Figure from *Mallick et al.* [2014].

## 4.2 RHESSI

RHESSI is the 6th mission in NASA's line of small explorer missions and was launched in February 2002 into a low earth orbit of 600km and a 38 degree inclination. It's primary mission objective is to explore the basic physics of particle acceleration and energy release in solar flares. However it also has science objectives that are classified as non-solar where they include the study of gamma-rays from terrestrial sources, TGFs [*NASA*, b].

### 4.2.1 Instrumentation

The mission is based around RHESSI's single instrument, the germanium crystal spectrometer, consisting of 9 germanium detectors. The germanium spectrometer can detect incoming X-rays from 3keV up to 20MeV gamma rays and incoming photons are converted into a measurable electrical current pulse proportional to the energy of the incoming photon [*Smith et al.*, 2002]. The standard operating temperature of the spectroscope is at around 90 K or -183 degrees Celsius. The spectrometer is designed to investigate the energy release and particle acceleration through the spectroscopy of hard X-rays/gamma-rays (3keV to 17MeV) produced by energetic electrons and ions in solar flares [**?**].

The internal clock on RHESSI has been found to run 1.8ms slower than UTC (Coordinated Universal Time) [*Grefenstette et al.*, 2009], and *Gjesteland et al.* [2014] found its uncertainty to be $\sim$ 0.1ms after 5th of August 2005 (will be discussed in Section 3.2).

### 4.2.2 The South Atlantic Anomaly

During transits over the South Atlantic Anomaly (SAA), RHESSI's Germanium spectrometer will turn itself off. This is due to the higher than normal flux of energetic particles which will damage the instrument, as a means to protect the instrument of prolonged exposure to this radiation. As a result, no data will be registered during these transits and lightning flashes from this region will have to be discarded.

### 4.2.3 Annealing

RHESSI's instrumentation is subject to deterioration over time, due to the light shielding of its Germanium detectors, it periodically requires maintenance in the form of annealing. This is done by heating up the detector to a temperature of 90°C/363K, well above its operating temperature of -183°C/90K, leaving the instrument to "soak" for a period of time [*Veres et al.*, 2009]. RHESSI performed its third anneal in January 2012, lasting from the 17th of January till the 22nd of February leaving the instrument non-functional during this time period, resulting in no available gamma-ray data for this period of time. This means that lightning data during this period of time will have to be discarded as well.

## 4.3 Finding Candidates

### 4.3.1 Course search

In 2012 WWLLN recorded $189 \times 10^6$ events, and in 2006 it recorded $52 \times 10^6$ events. We initially started with a rough search to discard all events outside RHESSI's FOV. In the rough search we compared every WWLLN registered lightning flash with RHESSI's position closest in time. We say "closest in time" as RHESSI only gives it's location every 20 seconds. Every flash occurring inside a 1000km FOV of RHESSI was saved, and the rest discarded.

This dramatically reduced the number of events we have to work with down to $1.5 \times 10^6$ and $0.4 \times 10^6$ for 2012 and 2006 respectively. This gives us a total of $\sim 2 \times 10^6$ for both years.

### 4.3.2 Fine search

The next step is to get an accurate position of RHESSI at the time of lightning. As RHESSI only gives its position every 20 seconds, we need to extrapolate the trajectory from the previous known point, until the next. This

is done with a simple linear extrapolation, where we extend RHESSI's trajectory in a straight line with its current velocity.

Next, each event was logged with the WWLLN time and location, the RHESSI location (extrapolated) at the time of the event, as well as the great circle between the flash and RHESSI's sub-satellite point. We also saved the light curves for the time and energy of incoming photons in these structures. The gamma-ray data were extracted in a $[-50\text{ms}, 50\text{ms}]$ window centred around the time of the event.

Discarding events from transit over the SAA and the 2012 RHESSI annealing further bring the number of events down to $\sim 920 \times 10^3$ and $\sim 350 \times 10^3$ for 2012 and 2006 respectively.

### 4.3.3 TGF Propagation time

Another issue we need to take into account is the travel time required by the photons from an altitude of around $\sim$ 10km at the lightning location, to RHESSI at an average altitude of $\sim$ 540km as well as the great circle distance between them. This time delay is typically of the order of $\sim$ 2ms but can be as high as $\sim$ 4ms. To find the exact time propagation for each individual event, we use the Earth-centred Inertial (ECI) coordinates of each event. ECI is a coordinate system with its origin at the centre of the earth, where the $x - y$ makes a plane with Earth's equator, and the $z$-axis extends through the north pole. We compared the ECI coordinates for each event with the ECI coordinates of RHESSI at the same time (This position is extrapolated from the position RHESSI gives every 20 seconds), and hence find the vector pointing from the event to RHESSI. The length of this vector is the distance the photons need to travel to reach the satellite. By using the equation $\delta t = d/c$ where $\delta t$ is the time, $d$ is the length of the vector, and $c$ being the speed of light, we can find the travel time of gamma-rays associated with each event. This can be seen in Figure 4.2.

The propagation time was calculated for each event and saved into the data structure.

As mentioned in Section 3.2, the internal clock of RHESSI also has a systematic error, resulting in the clock running approximately 1.8ms slower than

UTC [*Gjesteland et al.*, 2012; *Grefenstette et al.*, 2009]. This means that the time-tag of the photons must have 1.8ms added to them.

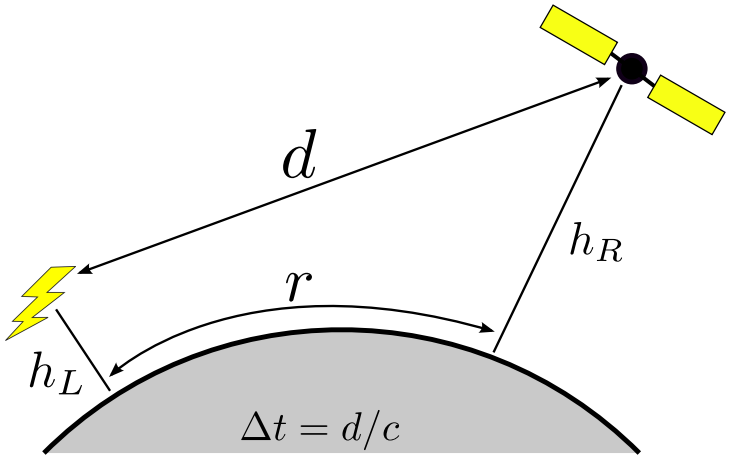


Fig. 4.2: Shows the distance $d$ between an event and RHESSI, along with the great circle distance between them, $r$. $\Delta t$ is the propagation time between the flash and the satellite.

## 4.4 Superposed light curves

To search for unidentified TGFs in this dataset, we can superpose the light curves for all the events. If there are weak TGFs in the data set, they will be indistinguishable from the background, but if we superpose thousands of events, they may become statistically significant. We will also look at the distribution of gamma-rays at the time of the event compared to the background gamma-ray distribution.

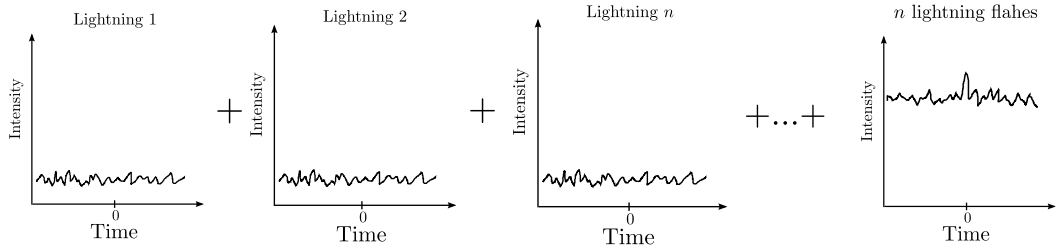


Fig. 4.3: Shows a simple illustration of how we hypothesize that the superposition of light curves can result in a statistical increase of gamma-rays at $t = 0$.

## 4.5 Testing and data selection

At this point we can start testing our data to see if everything up to this point is correct. As we have lightning data for two years, some of the entries contain data from actual TGFs. We can then combine the gamma-ray counts for all the lightning flashes that match the same time tags as the TGFs to get graph seen in Figure 4.4. As TGFs have a typical duration of $\sim 250\mu s$ [*Briggs et al.*, 2013] we are using a binsize of $300\mu s$. As the uncertainty of RHESSI's clock due to the systematic error is 0.1ms, we cannot use a binsize smaller than this range of error. Our binsize of $300\mu$s is well within this. In addition we have used a FOV of 800. The reason for this choice of FOV will be discussed in Section 6.3

Time at $t = 0$ is the time we expect the gamma-rays produced by lightning to hit the detector. This is done by calculating the travel time from the lightning flash to the detector and subtracting this from the actual data registered, in addition to adding the 1.8ms. As we can see from Figure 4.4 the search algorithm and time delays we have taken into account seems to work well, as we have a very large peak at $t = 0$ as well as some residual counts just to the left and right of the peak.

As already mentioned, during RHESSI's orbit around Earth, we want to exclude all lightning flashes that occur whenever RHESSI passes over the South American Anomaly (SAA) as well as all the lightning flashes happening during RHESSI's annealing in 2012. During these two conditions, the instrument is supposed to be turned off, registering no incoming gamma-rays. Figure 4.5 shows all the lightning events we have for 2012. This means

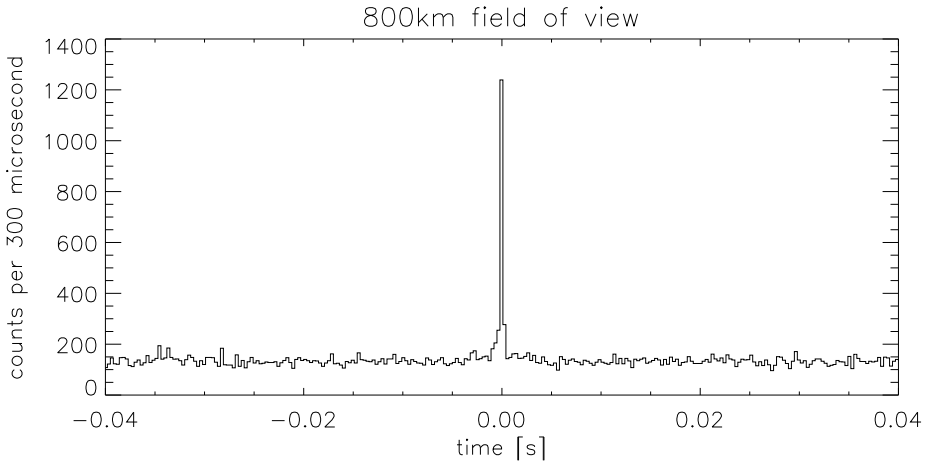


Fig. 4.4: Shows the counts per 300 $\mu s$ for every lightning event within 0.5 seconds of registered TGFs for the year 2006 and 2012. Time = 0 is the time we expect the gamma-rays to hit the detector.

that RHESSI was within 1000km of the lightning strike. Figure 4.6 shows the same thing, but we now have taken out where the instrument was turned off. As we can see, by only including the events where the instrument was turned on, we effectively remove every lightning strike occurring inside the SAA. The other events disappearing are due to the 2012 annealing and potentially other periods where RHESSI have no data.

After some more testing we noticed that some events produced an interesting result in the light curves. The general background noise for RHESSI is around 2 counts per milliseconds [*Grefenstette et al.*, 2009], however certain events occurred when the background before and after was far less than this, and some far more. We made an investigation into the distribution of background noise per event and put it into a histogram, seen in Figure 4.7. The figure shows the number of background counts RHESSI registered during the 100ms window we are looking at. As we can see we have a peak at 161 (1.61 per ms) counts, slightly less than the reported $\sim 2$ background counts per ms.

The reason for events with a higher than normal count rate is most likely RHESSI passing through the radiation belts (due configuration of the geomagnetic field) at high latitudes where there is a higher than normal particle flux. The lower than normal count rate might be due to the when RHESSI's

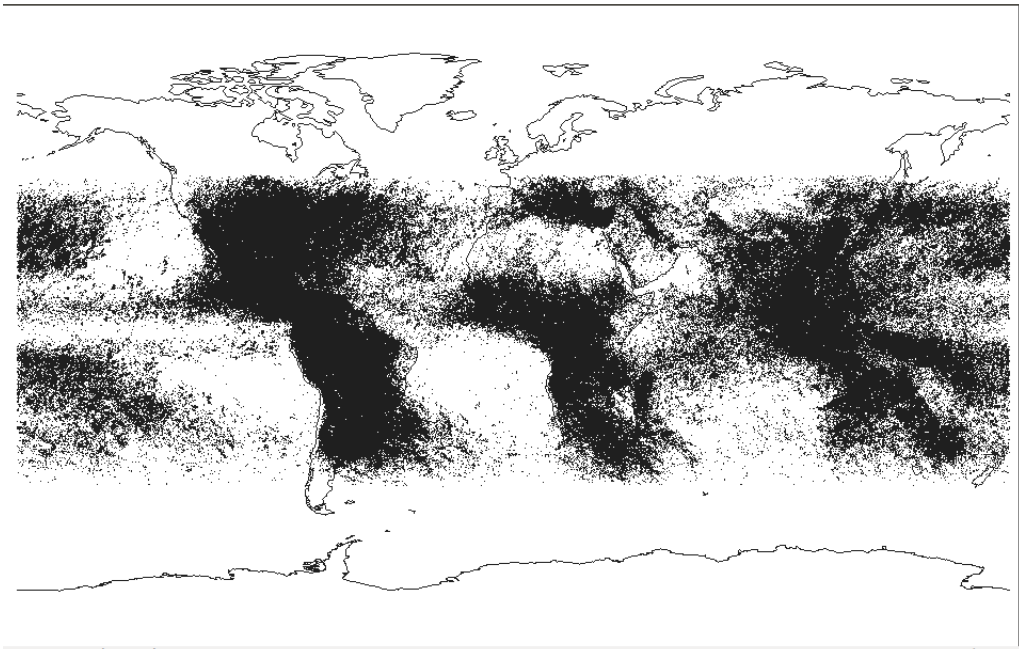

Fig. 4.5: Shows all the WWLLN registered lightning for 2012 that RHESSI is able to detect according to our methodology. Each of the black dots represents a lightning strike where RHESSI's sub-satellite was within 1000km.

instrument turns itself on or off before or after transit over the SAA, so that we only get a partially filled interval. It can also be due to certain glitches we have experienced, where data is simply missing in short time windows. Regardless we decided to only include events where the number of counts registered were between 100 and 300. This way we could exclude events with unusual background level.

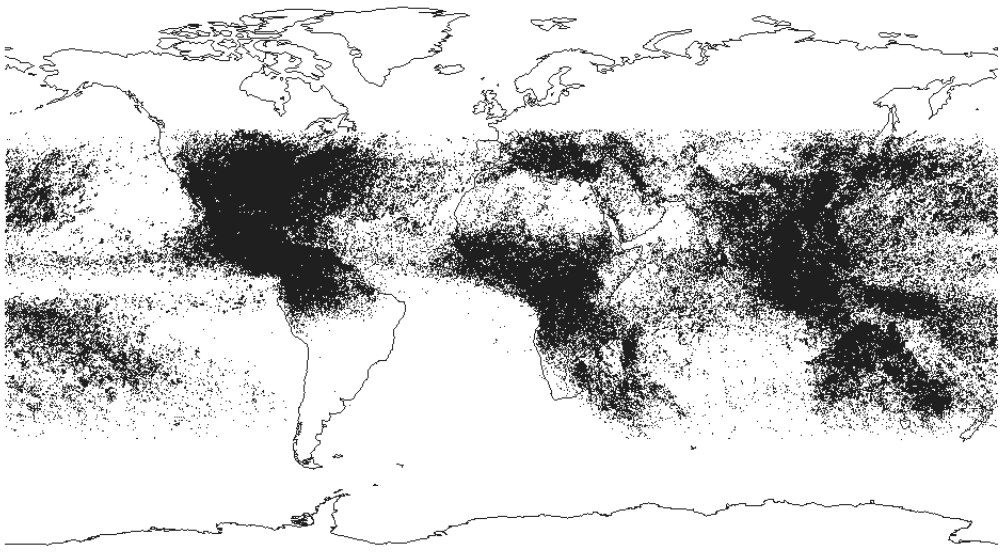

Fig. 4.6: Shows all WWLLN registered lightning flashes for 2012 that RHESSI is able to detect, as in Figure 4.5, but with times that RHESSI had no data taken out. This means lightning flashes occurring while RHESSI is over the SAA as well as under the annealing.

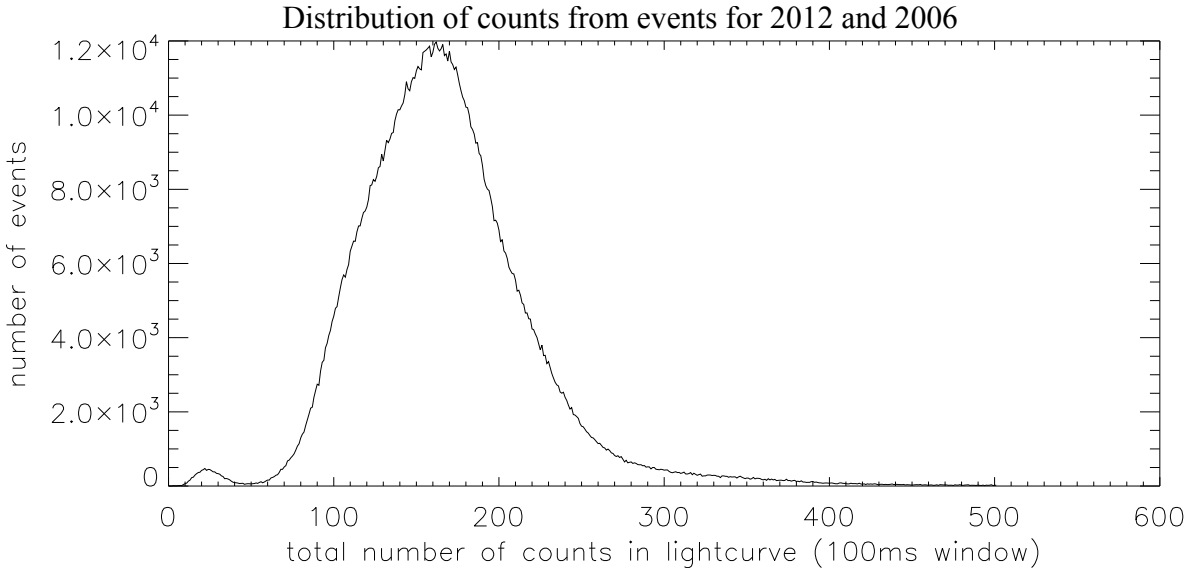


Fig. 4.7: Shows the distribution of counts registered in the 100ms window taken out of RHESSI after each lightning flash in 2006 and 2012.

# Chapter 5

# Results

In 2006 and 2012 WWLLN detected $\sim 52 \times 10^6$ and $\sim 189 \times 10^6$ lightning flashes respectively. By discarding events outside of RHESSI's FOV we end up with up with $1.52 \times 10^6$ events for 2012 and $0.40 \times 10^6$ events for 2006, giving almost 2 million lightning flashes detected by RHESSI over these two years. Removing the flashes happening during transit over the SAA and during the annealing cuts this down to $\sim \times 35010^3$ events for 2006 and $\sim 920 \times 10^3$ events for 2012. The final events we need to discard are the ones where we get an unusual large or unusual low number of background counts during the 100ms interval.

This brings us down to the number of events of $\sim 840 \times 10^3$ for 2012 and $\sim 330 \times 10^3$ for 2006 giving a total of $1.17 \times 10^6$ events total. what we can vary at this point is the FOV, and we have used a FOV of 800km. This choice will be discussed in Section 6.3. This brings the final number down to $\sim 540 \times 10^3$ and $\sim 210 \times 10^3$ for 2012 and 2006 respectively.

Figure 5.1 shows the gamma-ray data for 2012 and 2006 inside an 800km FOV. The peak has a sigma value of 4.71 by following the standard deviation calculation seen in Equations 5.1 to 5.3. This calculates the standard deviation by least mean squares.

$$Mean = \bar{x} = \frac{1}{N} \sum_{i=1}^{N-1} x_i \tag{5.1}$$

$$Variance = \frac{1}{N-1}\sum_{i=0}^{N-1}(x-\bar{x})^2 \tag{5.2}$$

$$Standard\ deviation = \sqrt{Variance} \tag{5.3}$$

Using the method in *Grefenstette et al.* [2009] and *Gjesteland et al.* [2012] where they estimate the sigma by Poisson statistics we arrive at a sigma of 5.00, slightly higher. In this method we assume a Poisson distribution, which means that the mean is equal to the variance and the expectation value, seen in Equation 5.4 where $\lambda$ is the mean, $E(x)$ is the expectation value and $Var(x)$ is the variance. This means that the standard deviation is equal to the square root of the mean, seen in Equation 5.5, and then it is only to see how many standard deviations above the mean the peak is.

$$\lambda = E(x) = Var(x) \tag{5.4}$$

$$\sigma = \sqrt{\lambda} \tag{5.5}$$

We can also look at the gamma-ray data from 2006 and 2012 individually, as can be seen in Figure 5.2 and Figure 5.3 respectively. The data from 2006 has a standard deviation of 3.64 sigmas, and the 2012 data of 3.27 by the least mean square method.

We can now look at the count distribution of the background in Figure 5.4, compared to that of the expectant Poisson distribution. We can do this by making a histogram of the number of background counts registered for each event. This can be seen in Figure 5.4, where the black histogram is the background, and the red histogram shows the expected background by Poisson distribution. The Poisson distribution indicates that the background is not perfectly Poisson distributed. The Poisson function has used an expectation value of 1.61 counts per milisecond as this is the value of the peak in Figure 4.7. This gives an expectation value of 0.48 counts per 300$\mu$s.

We can further investigate the peak in Figure 5.1 by looking at the distribution of counts. This can be seen in Figure 5.5. In this figure we have plotted the incoming gamma-rays for each event in black and the Poisson

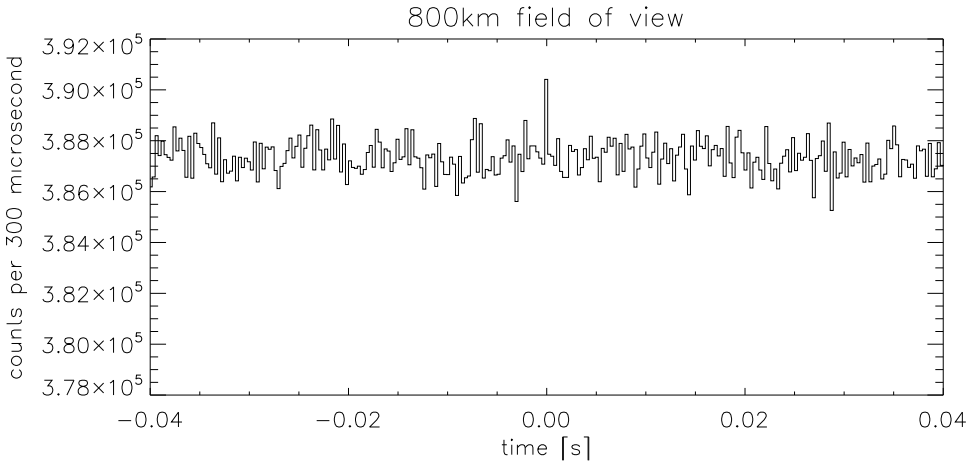


Fig. 5.1: Shows the combined data for $\sim 760 \times 10^3$ lightning flashes in 2006 and 2012, inside an 800km FOV. One should note that the y-axis does not start at zero.

distribution in red. The Poisson distribution shows the expected distribution of counts for the background. We used the same expectation value for the Poisson distribution as in Figure 5.6.

As we can see in Figure 5.4 the background does not follow a perfect Poisson distribution, but we can also plot the peak distribution and the background distribution on the same plot, to see the differences between the two. This is seen in Figure 5.6, where the peak distribution is given in black, and the background distribution in red. At $x = 5$ we can start seeing the difference between the two plots. At $x = 6$ and onwards it becomes clear that our dataset contains events with higher than normal background, possibly previously undiscovered TGFs.

If we take the counts from $x \geq 6$ and above in Figure 5.6 and subtract the background from the peak, we get that there are 223 events that cannot be explained by the background.

We also looked at the positioning of the 223 potential weak TGFs. We took every event that registered 6 or more counts in the peak bin and found how far away from the sub-satellite point the flash happened. Some of these are what we hypothesise are weak TGFs, but some will also be background, due to our inability to differentiate them. The distribution of their distance from

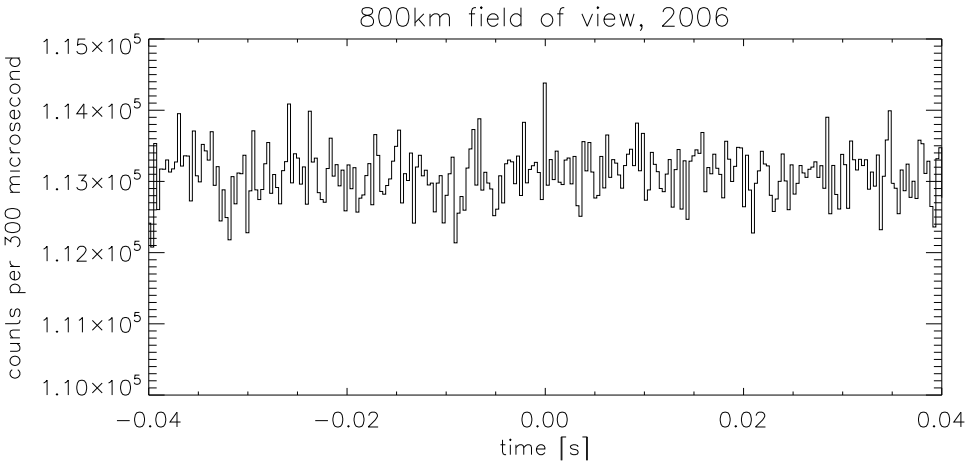


Fig. 5.2: Shows the combined data for $\sim 210 \times 10^3$ lightning flashes in 2006, inside an 800km footpoint. One should note that the y-axis does not start at zero.

the sub-satellite point can be seen in Figure 5.7.

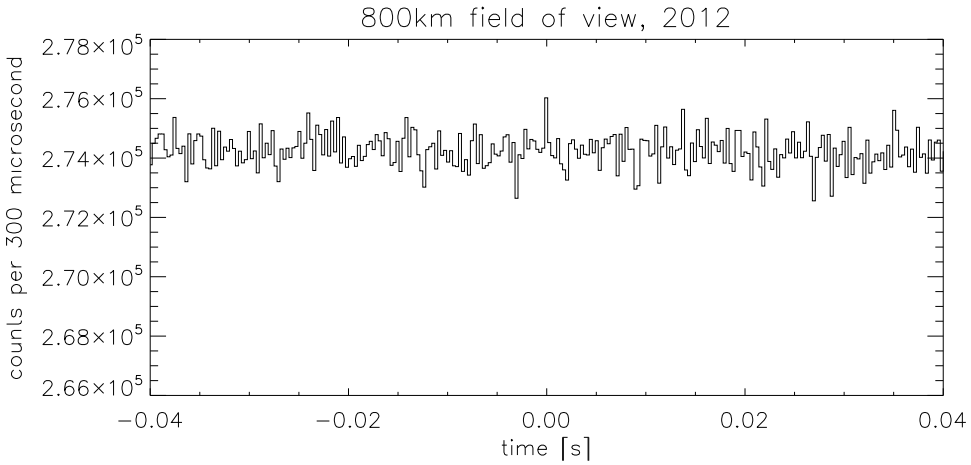


Fig. 5.3: Shows the combined data for $\sim 540 \times 10^3$ lightning flashes in 2012, inside an 800km footpoint. One should note that the y-axis does not start at zero.

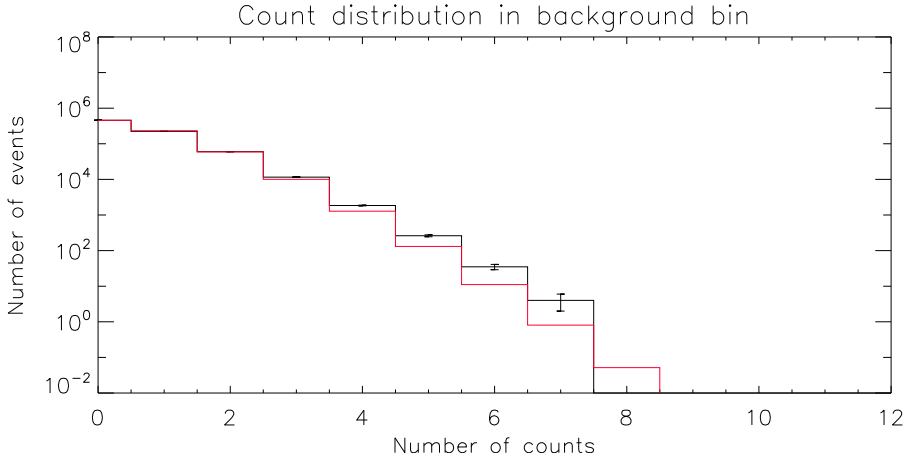


Fig. 5.4: Shows the number of events with different number of counts in a background bin in black. The red line is a Poisson distribution of the expected counts.

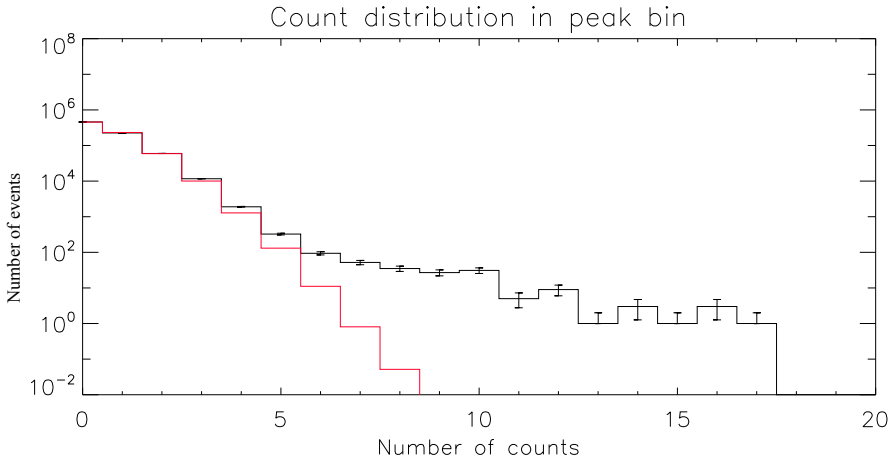


Fig. 5.5: Shows the number of events with different number of counts in the peak bin in black. The red line is a Poisson distribution of the expected counts. The bins with error bars only going upwards indicate that the uncertainty goes all the way down to zero, as the plot is logarithmic on the y-axis.

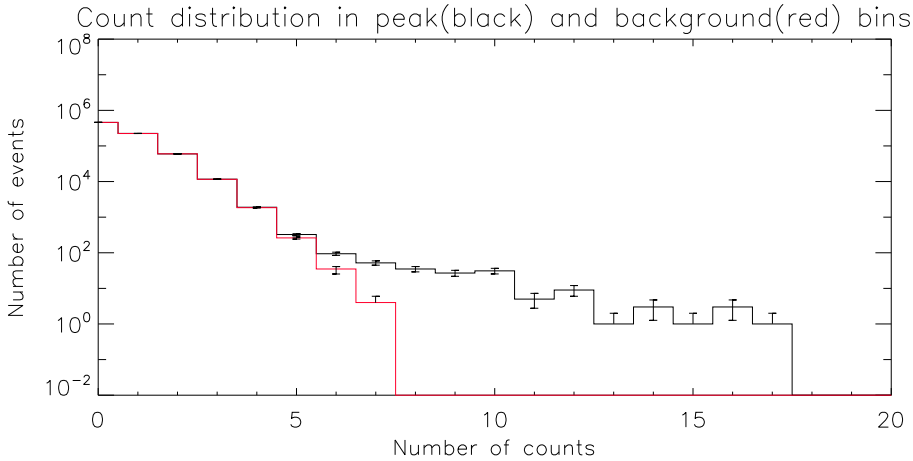


Fig. 5.6: Shows the number of events with different number of counts in the peak bin in black and the background in red. The bins with error bars only going upwards indicate that the uncertainty goes all the way down to zero, as the plot is logarithmic on the y-axis.

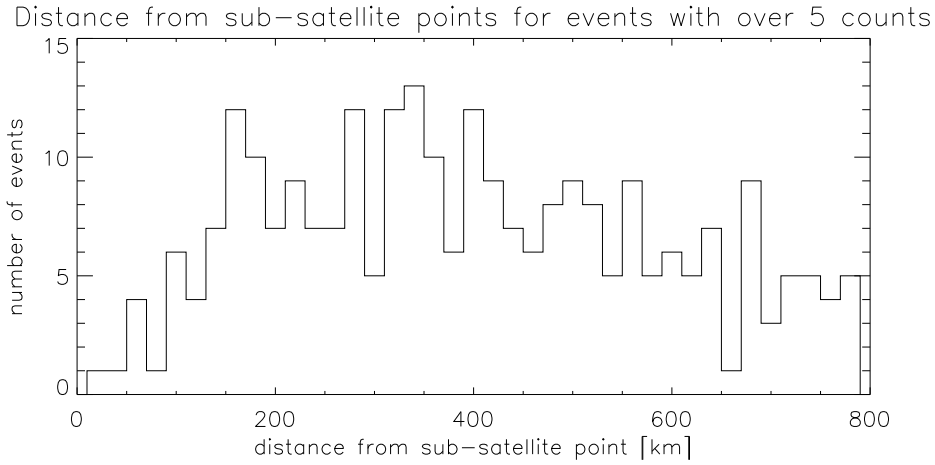


Fig. 5.7: Shows the distribution of the distance between lightning flashes and the sub-satellite point. All events here registered 6 counts or more in RHESSI. The binsize is 20km.

## 5.1 Curve fitting

As we can see in Figure 5.6 our gamma-ray distribution consists of the random background noise as well as an extra bit containing what we believe to be weak unidentified TGFs.

We can use a curve fit to model the distribution of gamma-rays in the peak bin. We compute non-linear least square fits of our function for an arbitrary number of parameters. The function can be any non-linear function as long as partial derivatives can be computed or approximated. We then iterate until the $\chi^2$ value approaches it's minimum value.

We do this by assuming a Poisson background and a power law TGF fluence distribution (see Section 3.6). We can then let the algorithm determine the constants in these functions to get the line of best fit. Equation 5.6 describes the Poisson distribution of the background, where $A_0$ is the scaling factor (as a poisson distribution determines probability, they all add up to 1. Since we're dealing with thousands of counts, we need to scale this to the total number of events). $A_1$ is the expectation value of the Poisson distribution. *Grefenstette et al.* [2009] gave a rough estimate of a background of $\sim$ 2 counts per millisecond, however according to our plot in Figure 4.7 we find that closer to 1.61 counts per ms is the expected background(The peak of the figure is at 161 counts over 100ms). This gives an expectation value of 0.48 counts per 300$\mu$s bin. By using the Curve Fitting function we can see if there is another value for the background that fits better with our results.

$$f(x) = \frac{A_0 A_1^X e^{-A_1}}{X!} \tag{5.6}$$

To use inbuilt equation we need to determine the partial derivatives of the equation with respect to the unknown constants. The partial derivative of Equation 5.6 with respect to $A_0$ can be seen in Equation 5.7.

$$\frac{\partial f}{\partial A_0} = \frac{A_1^X e^{-A_1}}{X!} \tag{5.7}$$

Doing the same but with respect to $A_1$ we arrive at the result seen in Equation

5.8

$$\frac{\partial f}{\partial A_1} = \frac{A_0}{X!}\left(X A_1^{X-1} e^{-A_1} - A_1^X e^{-A_1}\right) \tag{5.8}$$

The result in Equation 5.8 can be further simplified to Equation 5.9

$$\frac{\partial f}{\partial A_1} = \frac{A_0 A_1^X e^{-A_1}}{X!}\left(\frac{X}{A_1} - 1\right) \tag{5.9}$$

We can then use these partial derivatives in a curve fitting procedure. This works by a least means square fitting procedure minimizing the difference between the data and the predicted equation. The gamma-ray distribution of the background along with a fitted curve can be seen in Figure 5.8. The curve fitting gave a best with an $A_0 = 755328.28$ and $A_1 = 0.51$. The value of $A_0$ corresponds well to the real total number of events observed at 756137. $A_1$ is the expectation value of background per bin, and was found to be 0.51 per $300\mu s$. This is equivalent to 1.7 counts per millisecond, close to 1.61 counts per millisecond) we deduced from Figure 4.7.

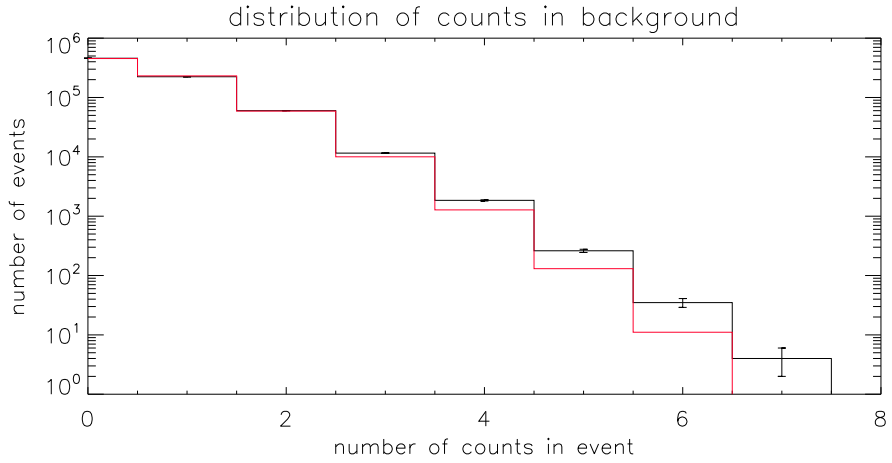


Fig. 5.8: Shows the number of events with different number of incoming gamma-rays (or counts) in the background bin in black and the curve fitted Poisson distribution in red.

If we assume that the possible faint TGFs in Figure 5.5 follow a power law distribution explained in *Østgaard et al.* [2012], we can use the same curve

fitting procedure to get a value for $\lambda$. This means we also need to include a power law term into Equation 5.6 to account for the distribution of TGFs. This power law is seen in Equation 5.10. $A_2$ is here a scaling factor and $A_3$ represents the value $\lambda$, the exponent in the power law function. This is a measure of the slope the fluence distribution follows.

$$f(x) = A_2 X^{-A_3} \tag{5.10}$$

To have the total distribution of the background noise and the TGF power law we combine Equation 5.6 and Equation 5.10 into Equation 5.11.

$$f(x) = \frac{A_0 A_1^X e^{-A_1}}{X!} + A_2 X^{-A_3} \tag{5.11}$$

We already have the first two partial derivatives in Equation 5.7 and Equation 5.9, and we need to determine the partial derivatives for $A_2$ and $A_3$. These can be seen in Equation 5.12 and Equation 5.13.

$$\frac{\partial f}{\partial A_2} = X^{-A_3} \tag{5.12}$$

$$\frac{\partial f}{\partial A_2} = -A_2 \; ln(X) X^{-A_3} \tag{5.13}$$

We can then put these partial derivatives into a curve fitting procedure to find the constants giving the best fit for our data, as can be seen in Figure 5.9. With the combined background and unidentified we get an $A_0$ value of 752756, and an $A_1$ value of 0.51, fitting well with the total number of events and the expectation value. We get the value of 1553 for $A_2$ and a value of 1.82 for $A_3$. It should be noted that due to the low number of events with counts $x \geq 13$ these have not been weighted in the curve fitting.

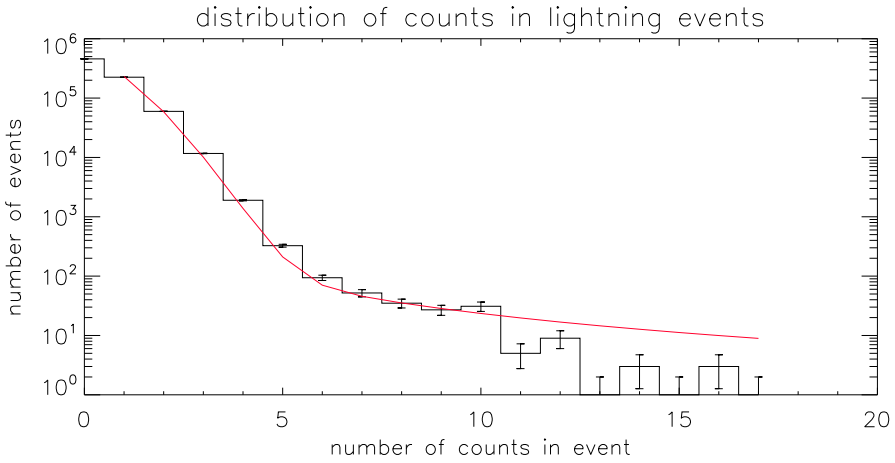


Fig. 5.9: Shows the number of events with different number of incoming gamma-rays (or counts) in the peak bin in black and the curve fitted for the background and TGFs in red. Due to the very low number of counts in $x \geq 13$ these have not been weighted for the fitting curve. This gives a $\lambda = 1.82$.

# Chapter 6

# Discussion

In this chapter we will discuss the results presented in Chapter 5, as well as their possible implications. We have found that at the time of lightning, there are in fact an increased number of counts registered by RHESSI. Our superposing of all lightning events gave us a result $5.0\sigma$ over the background. This is a strong indication of the existence of weaker TGFs than RHESSI's lower threshold.

## 6.1 Existence of weak TGFs

In the catalogue presented by *Grefenstette et al.* [2009], the emphasis was finding clear TGFs, with a very low probability of false positives. Therefore they used a conservative search algorithm requiring 17 counts over the background to register as a TGF. The algorithm used by *Gjesteland et al.* [2012] identifies TGFs down to 10 counts, as this algorithm is less conservative. The resultant TGFs from these algorithms can be seen in Figure 6.1.

Our result indicates that there are weaker TGFs in existence, that can be seen from around 5 counts in RHESSI. *Østgaard et al.* [2012] investigated the difference in sensitivity between RHESSI and the Fermi BGO. Taking into account their different inclination and detector sizes, they predicted the lower detection threshold of Fermi on RHESSI's scale of counts per TGFs. As Fermi has a larger detector than RHESSI, Fermi will detect more counts

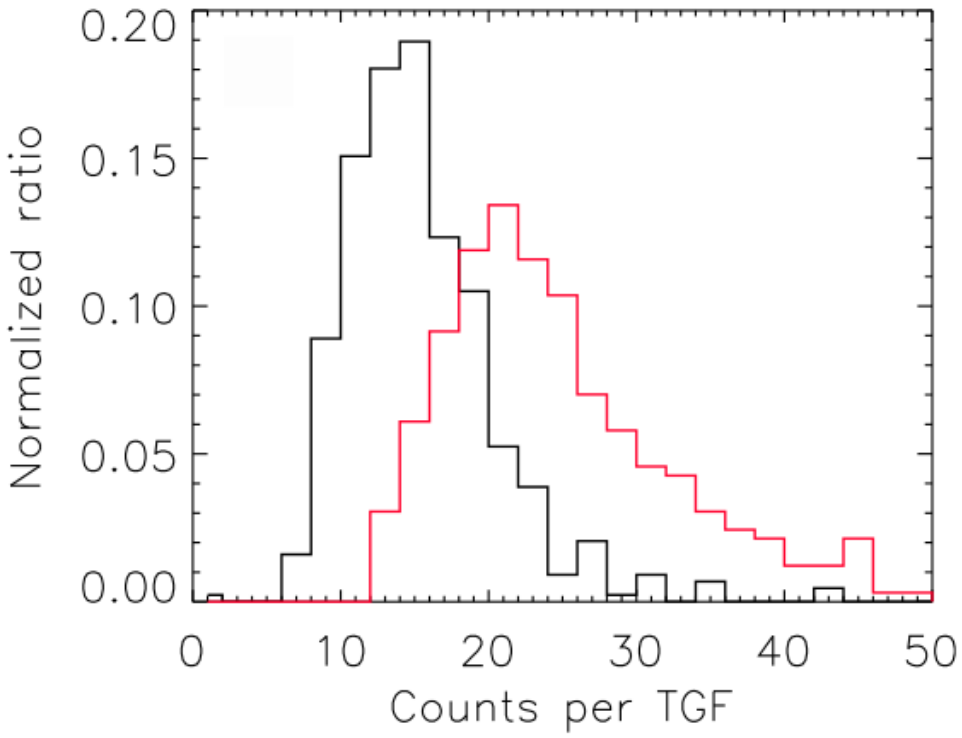


Fig. 6.1: Distribution of TGF intensity for year 2004, 2005 and 2006. The black is from 554 TGFs from *Gjesteland et al.* [2012] and the red is 474 TGFs from *Grefenstette et al.* [2009].

than RHESSI in the same TGF. As a result, *Østgaard et al.* [2012] found Fermi's lower detection threshold on RHESSI's scale to be 6.3 counts per TGF. This means that the weakest TGFs Fermi can detect, corresponds to 6.3 counts in RHESSI.

This supports our argument that there are weaker TGFs undetectable by RHESSI.

## 6.2 The fluence of weak TGFs

We also modelled the fluence of our weak TGFs after a power law of the form $Ax^{-\lambda}$ as can be seen in Figure 5.9. It has been suggested in several

papers that the fluence distribution of TGFs follow a power law of this form *Østgaard et al.* [2012]; *Marisaldi et al.* [2014]; *Tierney et al.* [2013].

*Østgaard et al.* [2012] found the $\lambda$ in this power law relationship to be $\lambda = 2.3$, where *Marisaldi et al.* [2014] found $\lambda = 2.4$ and *Tierney et al.* [2013] found $\lambda = 2.2$. Our value of $\lambda = 1.82$ is lower than this, however, *Østgaard et al.* [2012] also suggested the possibility of a roll-off in this power law (also called a broken power law by *Marisaldi et al.* [2014]). This roll off would be on the lower end of the fluence distribution, seen by the red line in Figure 3.5(b), where we have found our possible weak TGFs.

*Østgaard et al.* [2012] predicts this roll-off power law to have $\lambda = 1.7$ and *Marisaldi et al.* [2014] found the same value. This is closer to the value we found for $\lambda = 1.82$. This seems to indicate that there is a roll-off. According to *Østgaard et al.* [2012] this means that we cannot rule out that all lightning flashes produce TGFs.

## 6.3 Field of view choice

When trying to identify weaker TGFs, we believe that it is more constructive to widen the FOV of RHESSI to try to find them further away from the sub-satellite point, rather than deeper in the cloud. This is due to two reasons. TGF happening 800km from the sub-satellite point versus a TGF at 300km will be 7 times fainter due to the gamma-rays falling off as the intensity if proportional to $\frac{1}{r^2}$ and $\left(\frac{800}{300}\right)^2 \simeq 7$. The $300km$ comes from *Connaughton et al.* [2010] where they found no WWLLN matches with Fermi outside a 300km FOV. Trying to detect TGFs produced deeper in the atmosphere is harder as the intensity of them are proportional to the density of air. Figure 6.2 gives an indication of this. If we as an example take the two red circles on the line of weakest TGFs. A TGF coming from 10km versus 12km will have to be about an order of magnitude stronger to be detected with the same intensity as one from 12km. As a result, we believe we have a much higher chance of seeing TGFs further out from the sub-satellite point rather than deeper in the atmosphere.

Another point is the larger number of events possible by extending the radius. Increasing the radius from the sub-satellite point from 300 to 800 will yield

and area that is 7 times greater. If we assume a uniform distribution of TGFs (though this is not the case in reality) this will increase the number of possible faint TGFs by 7 times.

The reason we use a radius around the sub-satellite point of 800km and not larger of say 1000km, is that this did not produce a better result. On the contrary, going all the way to 1000km gave us a peak with a lower sigma value. This is probably due to the potential TGFs being too weak, as well as we are adding a large amount of background by including this. As we can see from Figure 5.7 there is a significant amount of events further out than 300km.

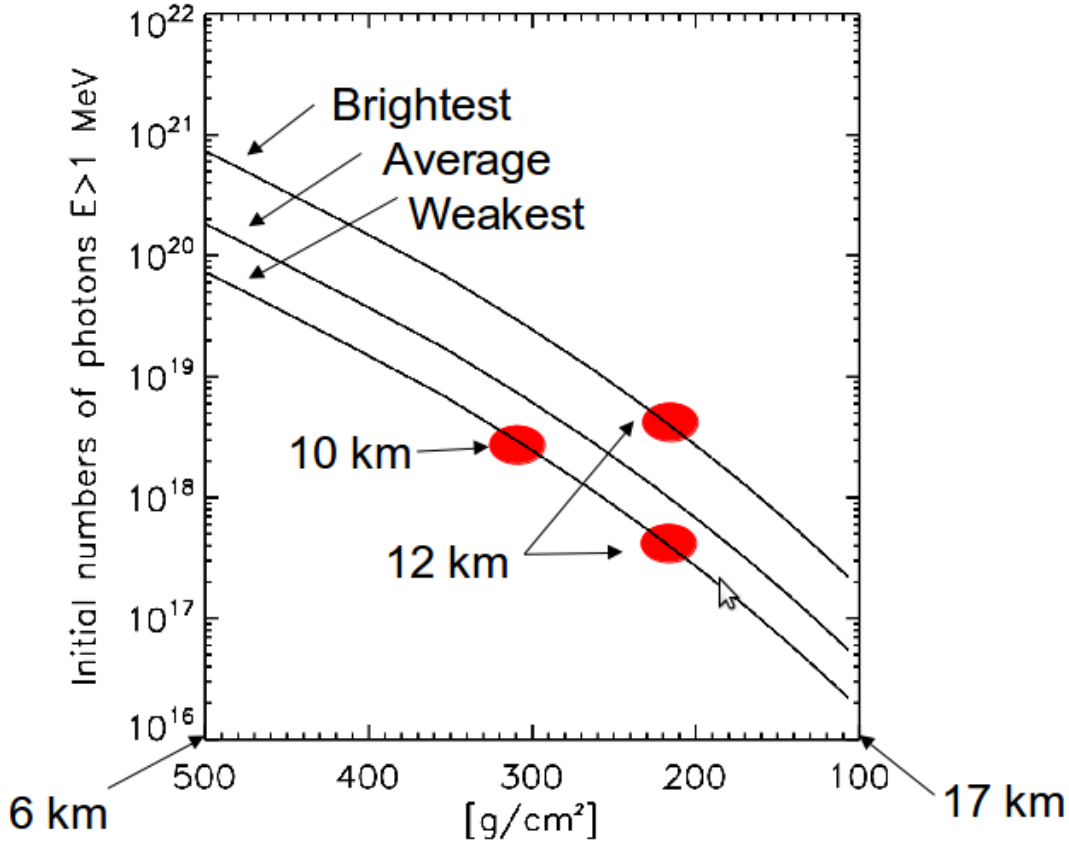


Fig. 6.2: Estimation of initial number of photons in a TGF based on RHESSI's brightest, average, and weakest TGF. Figure from *Gjesteland et al.* [2013].

## 6.4 Error calculations

### 6.4.1 WWLLN position uncertainty

According to *Østgaard et al.* [2013], WWLLN has a time uncertainty of 45$\mu$s, and a location uncertainty of $\sim$ 15km. If the flash happens directly under the satellite, the effect is negligible. Figure 6.3 illustrates this. The maximum error we can have from the WWLLN position is if a flash positioned at 800km is actually at 815km away. The difference in $d_1$ and $d_2$ determines how much longer gamma-rays from the flash further away must travel to reach RHESSI. To calculate the values for $d_1$ and $d_2$ we can use the Cosine rule in Equation 6.1.

$$c^2 = a^2 + b^2 - 2abcos(C) \tag{6.1}$$

Assuming that the radius of the Earth $R_{Earth} = 6370$ and the height of RHESSI $H_{RHESSI} = 527km$ (This is the lowest altitude of RHESSI in the data, as a lower altitude will yield a larger error), we find that $d_1 = 990$km and $d_2 = 1000$km, a difference of 10km. So due to WWLLN's position uncertainty, the largest possible error we can have due to this is 33$\mu$s.

In addition we have to take into account the time uncertainty. In our example seen in Figure 6.3 the flash happens 15km further away from RHESSI than reported by WWLLN. If the majority of the WWLLN detectors are located on the other side of the flash (so that the flash is between the majority of the WWLLN detectors and the sub-satellite point of RHESSI), the flash actually happened 45$\mu$s after that reported by WWLLN. As a result we need to add the time uncertainty of WWLLN of 45$\mu$s and the uncertainty in propagation time due to the position error of 33$\mu$s, giving a total uncertainty of 78$\mu s$. This is only in the most extreme cases.

### 6.4.2 Flash altitude

Another source of error is our assumption that all lightning flashes happen at 10km altitude. This was an assumption made earlier, as WWLLN does not give an altitude estimation. As we assume the TGF producing

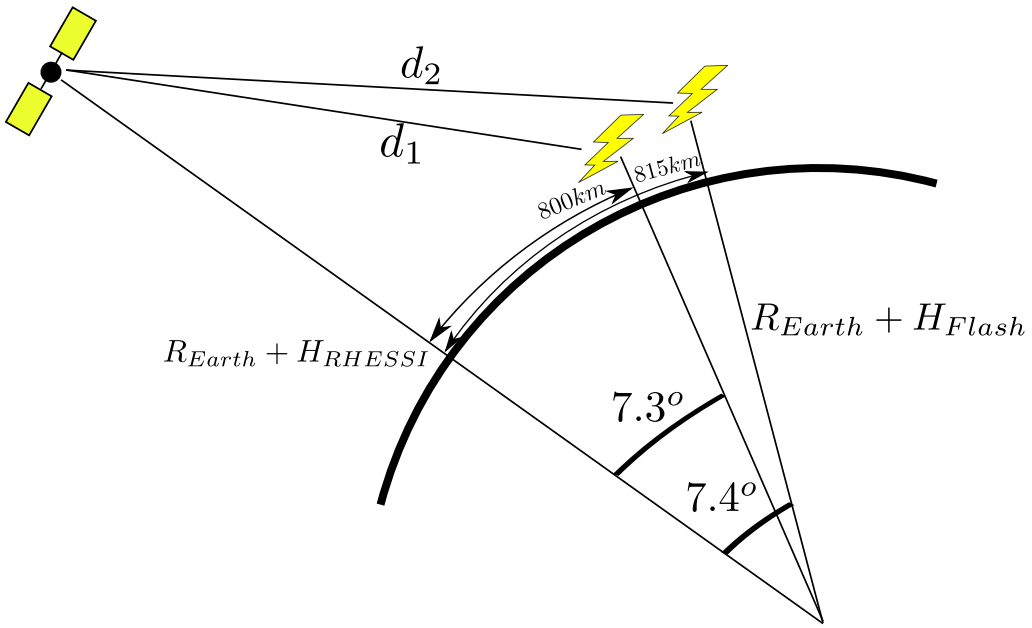


Fig. 6.3: Shows the position of a lightning flash 800km away from RHESSI's sub-satellite point, as well as a flash 15km further out (as this is the max error). The difference in $d_1$ and $d_2$ determines the maximum time error we have in RHESSI due to WWLLN's position uncertainty.

lightning flashes are positive IC flashes, we assigned them all an altitude of 10km. According to *Dwyer and Smith* [2005], the production altitude is somewhere between 15-21km. This means we can have up to a 6km error, if the flash happens directly under the satellite (for reasons similar to that of the WWLLN uncertainty, this error will get smaller the further away from the sub-satellite point the flash is). If we assume the maximum error here is 6km, this corresponds to a time of 20$\mu$s

The error in the WWLLN position and the flash altitude cannot be added together, as one is at minimum while the other at maximum and vice versa.

### 6.4.3 RHESSI extrapolation

We can also look at the error when we extrapolate the trajectory of RHESSI between the points where its position is given. As we extrapolate from one

point, the maximum error is when the satellite approaches the next position giving point as the extrapolation assumes a straight line and not the spherical path the satellite covers. We found that the maximum error from this is $\Delta d \sim 2$km. This means that close to the next position point, we assume the satellite to be $\sim 2$km higher than it really is. This yields a very small time error of $\sim 7\mu$s at most.

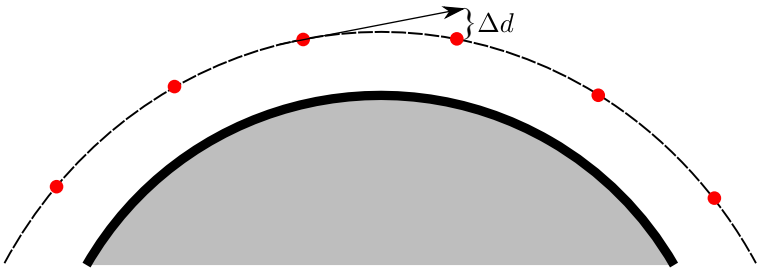


Fig. 6.4: Shows the extrapolation of RHESSI's trajectory between its positions. The red dots indicate the places where RHESSI gives it's position, and the arrow indicates the direction of extrapolation. $\Delta d$ is the vertical distance between the next position and the maximum height of the extrapolated trajectory.

### 6.4.4 RHESSI transit during photon propagation

There is also the fact that when we have a WWLLN flash and RHESSI's position, we calculate the propagation time of potential gamma-rays between them. During this propagation time, the satellite will continue to move at 7km $s^{-1}$. The longest propagation times are flashes at the furthest distance out of 800km, where the propagation time is $\sim$ 3.3ms. This means that RHESSI has moved another 23 meters during the time it takes for the gamma-rays to travel from it's source to the satellite, which means we can neglect this effect with ease.

### 6.4.5 RHESSI clock uncertinty

All of these errors are negligible compared to the uncertainty in RHESSI's clock of 100$\mu$s, and can therefore be ignored. The only exception is possibly

the 78$\mu$s uncertainty due to WWLLN's time and location uncertainty, but this is a varying uncertainty depending on the location of the lightning flash in relation to the sub-satellite point. Only in the most extreme cases will this uncertainty be 78$\mu$s, giving a total of 178$\mu$s.

As we have chosen a binsize of 300$\mu$s we believe the uncertainty in RHESSI's clock and the WWLLN uncertainty has a negligible effect on our results.

## 6.5 Improvements

### 6.5.1 CG and IC

In Figure 5.1 we see that we have a clear peak over the background, indicating an increase in gamma-rays hitting the detector at the time of lightning. However, noticing that the plot does not start at zero, there is in fact a very high level of background on the plot. This is due to WWLLN's inability to differentiate between IC and CG lightning flashes. It is estimated that 75% of all lightning flashes are of the IC type [*Boccippio et al.*, 1999], and it is currently predicted that it is the IC type that is producing TGFs.

However, WWLLN has a larger detection efficiency towards detecting CG flashes than IC flashes. According to *Abarca et al.* [2010] WWLLN had a CG detection efficiency of 3.88% and an IC detection efficiency of 1.78% in 2006-2007. In 2008-2009 these numbers rose to 10.30% and 4.82% respectively. We can then make a quick calculation to show the fraction of CG and IC in our data set, seen in Table 6.1. We see that in our data set, $\sim 2/5$ of our events are CG flashes that do not contribute to faint TGFs.

| Type | Relative occurrence | Relative detection rate | Relative occurrence in data set | Fraction in dataset |
|---|---|---|---|---|
| IC | 3 | 1 | 3 | 3/5 |
| CG | 1 | 2 | 2 | 2/5 |

Table 6.1: Shows the calculations for fractions of IC and CG in our data set. Relative occurrence is multiplied with relative detection rate to find the relative occurance in the data set of CG and IC flashes.

However, it should be noted that according to *Cummer et al.* [2011]; *Connaughton et al.* [2013]; *Østgaard et al.* [2013] the TGFs themselves are producing detectable VLF signals. This could mean that the WWLLN detection rate of TGF producing lightning flashes are higher than regular IC flashes. It is however difficult to say if this still applies to the possible weak TGFs we are investigating here.

### 6.5.2 Count distribution

If we look back to Figure 4.7 we previously explained that we discarded all events with more than 300 counts or less than 100 events. In hindsight this may not have been the best choice. The numbers were chosen somewhat arbitrarily, and if we instead chose a range of [70-270] we could have isolated more of the peak. Our start at 100 counts excludes a somewhat large portion of events due to the sharp raise of the plot between x = 70 and x = 100.

# Chapter 7

# Summary

We have taken WWLLN data from 2006 and 2012, identified all lightning flashes happening inside an 800km FOV of RHESSI. We then extracted the light curves in a 100ms window centred around the time of lightning (corrected for the propagation time and the systematic error in RHESSI) and superposed all the light curves.

We found that at the time of lightning, there is an increase in counts, $5\sigma$ over the background. This indicates that there are weaker unidentified TGFs that current algorithms are unable to identify due to them being indistinguishable from the background. There were in total $\sim 220$ events with counts $\geq 6$ where the majority of them cannot be explained by the random background.

We also made an attempt to fit these possible weak TGFs to a power law of the form $Ax^{-\lambda}$, where we found $\lambda = 1.82$. This is somewhat consistent with a roll-off fluence distribution suggested by *Østgaard et al.* [2012] where he suggest that the roll-off part of the power function has a $\lambda = 1.7$. Their findings were consistent with findings from *Marisaldi et al.* [2014]. According to *Østgaard et al.* [2012] this could indicate that all lightning flashes are associated with TGFs.

# Chapter 8

# Future Work

When performing this study, we only had access to WWLLN data from the years 2006 and 2012. Including all the years in between as well as extending the data to 2015 would give a lot more data, and we believe it would further strengthen our result. Having more data would also serve to improve the fit we can make for the power law relationship of the true fluence distribution.

There is also the need to study these new TGFs to see if they have any specific characteristics by themselves, and the nature of their energy spectra. By finding their distance from the sub-satellite point we can also strengthen our assertion that using a wider FOV is generally a better solution to finding weak TGFs than trying to find them deeper.

There is also work to be done to see how high the peak in Figure 5.1 varies with varying FOV. Through some simple trial and error we found at 1000km and 500 gave a lower number if $\sigma$ than 800, indicating that our $\sigma$ value peaks at a certain FOV size.

It would also be useful to use the entire background in the light curves to estimate the background count distribution. We were unable to use the entire background due to computational limitations.

# Bibliography


Abarca, S. F., K. L. Corbosiero, and T. J. Galarneau (2010), An evaluation of the Worldwide Lightning Location Network (WWLLN) using the National Lightning Detection Network (NLDN) as ground truth, *Journal of Geophysical Research: Atmospheres*, *115*(18), 1–11, doi:10.1029/2009JD013411.

Appleton, E. V., and M. A. F. Barnett (1925), On Some Direct Evidence for Downward Atmospheric Reflection of Electric Rays, *Proceedings of the Royal Society of London*, *109*(752), doi:10.1098/rspa.1925.0149.

Babich, L. P., E. N. Donskoy, I. M. Kutsyk, and R. a. Roussel-Dupré (2005), The feedback mechanism of runaway air breakdown, *Geophysical Research Letters*, *32*(9), 1–5, doi:10.1029/2004GL021744.

Boccippio, D. J., K. Cummins, H. J. Christian, and S. J. Goodman (1999), Combined Satellite and Surface-Based Estimation of the Intracloud/Cloud-to-Ground Lightning Ratio Over the Continental United States, pp. 108–122, doi:10.1175/1520-0493(2001)129⟨0108:CSASBE⟩2.0.CO;2.

Briggs, M. S., et al. (2010), First results on terrestrial gamma ray flashes from the Fermi Gamma-ray Burst Monitor, *Journal of Geophysical Research: Space Physics*, *115*(7), 1–14, doi:10.1029/2009JA015242.

Briggs, M. S., et al. (2013), Terrestrial gamma-ray flashes in the Fermi era: Improved observations and analysis methods, *Journal of Geophysical Research: Space Physics*, *118*(6), 3805–3830, doi:10.1002/jgra.50205.

Carlson, B. E., N. G. Lehtinen, and U. S. Inan (2009), Terrestrial gamma ray flash production by lightning current pulses, *Journal of Geophysical Research: Space Physics*, *114*(12), doi:10.1029/2009JA014531.

Carlson, B. E., T. Gjesteland, and N. Østgaard (2011), Terrestrial gamma-ray flash electron beam geometry, fluence, and detection frequency, *Journal of Geophysical Research: Space Physics*, *116*(11), 1–7, doi:10.1029/2011JA016812.

Celestin, S., and V. P. Pasko (2011), Energy and fluxes of thermal runaway electrons produced by exponential growth of streamers during the stepping of lightning leaders and in transient luminous events, *Journal of Geophysical Research: Space Physics*, *116*(3), 1–14, doi:10.1029/2010JA016260.

Cohen, M. B., U. S. Inan, R. K. Said, and T. Gjestland (2010), Geolocation of terrestrial gamma-ray flash source lightning, *Geophysical Research Letters*, *37*(2), 1–5, doi:10.1029/2009GL041753.

Coleman, L. M., and J. R. Dwyer (2006), Propagation speed of runaway electron avalanches, *Geophysical Research Letters*, *33*(11), 1–4, doi:10.1029/2006GL025863.

Connaughton, V., et al. (2010), Associations between Fermi Gamma-ray Burst Monitor terrestrial gamma ray flashes and sferics from the World Wide Lightning Location Network, *Journal of Geophysical Research: Space Physics*, *115*(12), A12,307, doi:10.1029/2010JA015681.

Connaughton, V., et al. (2013), Radio signals from electron beams in terrestrial gamma ray flashes, *Journal of Geophysical Research: Space Physics*, *118*(5), 2313–2320, doi:10.1029/2012JA018288.

Cooray, V. (2008), *The Lightning Flash*, 574 pp., Institute of Electrical and Electronic Engineers, doi:10.1049/PBPO034E.

Cummer, S. a., Y. Zhai, W. Hu, D. M. Smith, L. I. Lopez, and M. a. Stanley (2005), Measurements and implications of the relationship between lightning and terrestrial gamma ray flashes, *Geophysical Research Letters*, *32*(8), 1–5, doi:10.1029/2005GL022778.

Cummer, S. a., G. Lu, M. S. Briggs, V. Connaughton, S. Xiong, G. J. Fishman, and J. R. Dwyer (2011), The lightning-TGF relationship on microsecond timescales, *Geophysical Research Letters*, *38*(14), 1–6, doi:10.1029/2011GL048099.

Dowden, R. L., J. B. Brundell, and C. J. Rodger (2002), VLF lightning location by time of group arrival (TOGA) at multiple sites, *Journal of Atmospheric and Solar-Terrestrial Physics*, *64*(7), 817–830, doi:10.1016/S1364-6826(02)00085-8.

Dwyer, J. R. (2003), A fundamental limit on electric fields in air, *Geophysical Research Letters*, *30*(20), 2055, doi:10.1029/2003GL017781.

Dwyer, J. R., and D. M. Smith (2005), A comparison between Monte Carlo simulations of runaway breakdown and terrestrial gamma-ray flash observations, *Geophysical Research Letters*, *32*(22), 1–4, doi:10.1029/2005GL023848.

Dwyer, J. R., D. M. Smith, and S. a. Cummer (2012), High-energy atmospheric physics: Terrestrial gamma-ray flashes and related phenomena, *Space Science Reviews*, *173*(1-4), 133–196, doi:10.1007/s11214-012-9894-0.

Fishman, G. J., et al. (1994), Discovery of intense gamma-ray flashes of atmospheric origin., *Science (New York, N.Y.)*, *264*(5163), 1313–1316, doi:10.1126/science.264.5163.1313.

Fuschino, F., et al. (2011), High spatial resolution correlation of AGILE TGFs and global lightning activity above the equatorial belt, *Geophysical Research Letters*, *38*(14), 4–9, doi:10.1029/2011GL047817.

Gjesteland, T., N. Østgaard, a. B. Collier, B. E. Carlson, C. Eyles, and D. M. Smith (2012), A new method reveals more TGFs in the RHESSI data, *Geophysical Research Letters*, *39*(5), n/a–n/a, doi:10.1029/2012GL050899.

Gjesteland, T., N. Østgaard, M. Marisaldi, F. Fuschino, E. Arnone, S. Laviola, and A. Collier (2013), Terrestrial Gamma ray Flashes from low clouds over the Mediterranean sea.

Gjesteland, T., N. Østgaard, R. Nisi, A. Collier, and G. Lu (2014), Twelve Years of RHESSI TGFs The second RHESSI TGF catalog ., *EGU general assembly*, *16*, 14,125, doi:10.1029/2011JA016612.

Grefenstette, B. W., D. M. Smith, B. J. Hazelton, and L. I. Lopez (2009), First RHESSI terrestrial gamma ray flash catalog, *Journal of Geophysical Research: Space Physics*, *114*(2), A02,314, doi:10.1029/2008JA013721.

Griffiths, D. J., and C. Inglefield (2005), *Introduction to Electrodynamics*, vol. 73, fourth edi ed., 574 pp., doi:10.1119/1.4766311.

Gurevich, A. (1961), On the theory of run-away electrons, *Journal of Nuclear Energy (1954)*, *12*(5), 302, doi:10.1016/0891-3919(58)90187-6.

Inan, U. S., and N. G. Lehtinen (2005), Production of terrestrial gamma-ray flashes by an electromagnetic pulse from a lightning return stroke, *Geophysical Research Letters*, *32*(19), 1–5, doi:10.1029/2005GL023702.

Inan, U. S., S. C. Reising, G. J. Fishman, and J. M. Horack (1996), On the association of terrestrial gammaray bursts with lightning and implications for sprites, *Geophysical Research Letters*, *23*(9), 1017, doi:10.1029/96GL00746.

Inan, U. S., M. B. Cohen, R. K. Said, D. M. Smith, and L. I. Lopez (2006), Terrestrial gamma ray flashes and lightning discharges, *Geophysical Research Letters*, *33*(18), 2–6, doi:10.1029/2006GL027085.

Jayaratne, E., and C. Saunders (1983), Charge on ice crystals in laboratory clouds, *Journal of Geophysical ...*, (3), 5494–5496.

Jayaratne, E. R. (1998), Possible laboratory evidence for multipole electric charge structures in thunderstorms, *Journal of Geophysical Research*, *103*(D2), 1871, doi:10.1029/97JD02553.

Lehtinen, N. G., M. Walt, U. S. Inan, T. F. Bell, and V. P. Pasko (1996), y-ray emission produced by a relativistic beam of runaway, *Geophysical Research Letters*, *23*(19), 2645–2648.

Lu, G., et al. (2010), Lightning mapping observation of a terrestrial gamma-ray flash, *Geophysical Research Letters*, *37*(11), 1–5, doi:10.1029/2010GL043494.

Mallick, S., et al. (2014), Evaluation of the GLD360 performance characteristics using rocket-and-wire triggered lightning data, *Geophysical Research Letters*, *41*(10), 3636–3642, doi:10.1002/2014GL059920.

Marisaldi, M., et al. (2010), Detection of terrestrial gamma ray flashes up to 40 MeV by the AGILE satellite, *Journal of Geophysical Research*, *115*, A00E13, doi:10.1029/2009JA014502.

Marisaldi, M., F. Fuschino, M. Tavani, S. Dietrich, C. Price, M. Galli, C. Pittori, and F. Verrecchia (2014), Journal of Geophysical Research : Space Physics Properties of terrestrial gamma ray flashes detected by AGILE MCAL below 30 MeV, (November 2009), 1337–1355, doi: 10.1002/2013JA019301.Received.

Marshall, T. C., M. P. McCarthy, and W. D. Rust (1995), Electric field magnitudes and lightning initiation in thunderstorms, *Journal of Geophysical Research*, *100*(D4), 7097–7103, doi:10.1029/95JD00020.

Moss, G. D., V. P. Pasko, N. Liu, and G. Veronis (2006), Monte Carlo model for analysis of thermal runaway electrons in streamer tips in transient luminous events and streamer zones of lightning leaders, *Journal of Geophysical Research: Space Physics*, *111*(2), 1–37, doi:10.1029/2005JA011350.

NASA (a), NASA website: Gamma-ray Astrophysics.

NASA (b), NASA website: About the RHESSI mission.

Nemiroff, R. (1997), Temporal and spectral characteristics of terrestrial gamma flashes, *Journal of Geophysical ...*, *102*(96), 9659–9665.

Østgaard, N., T. Gjesteland, R. S. Hansen, a. B. Collier, and B. Carlson (2012), The true fluence distribution of terrestrial gamma flashes at satellite altitude, *Journal of Geophysical Research*, *117*(A3), A03,327, doi: 10.1029/2011JA017365.

Østgaard, N., T. Gjesteland, B. E. Carlson, a. B. Collier, S. a. Cummer, G. Lu, and H. J. Christian (2013), Simultaneous observations of optical lightning and terrestrial gamma ray flash from space, *Geophysical Research Letters*, *40*(10), 2423–2426, doi:10.1002/grl.50466.

Rakov, V., and M. Uman (2003), *Lightning: physics and effects*.

Rodger, C., and J. Brundell (2004), Location accuracy of long distance VLF lightning locationnetwork, *Annales ...*, pp. 747–758.

Rodger, C. J. ., C. J. . Rodger, J. B. . Brundell, J. B. . Brundell, R. Holzworth, R. Holzworth, E. Lay, and E. Lay (2009), Growing Detection Efficiency of the World Wide Lighting Location Network.

Rudlosky, S. D., and D. T. Shea (2013), Evaluating WWLLN performance relative to TRMM/LIS, *Geophysical Research Letters*, *40*(10), 2344–2348, doi:10.1002/grl.50428.

Shao, X. M., T. Hamlin, and D. M. Smith (2010), A closer examination of terrestrial gamma-ray flash-related lightning processes, *Journal of Geophysical Research: Space Physics*, *115*(6), 1–8, doi:10.1029/2009JA014835.

Smith, D., L. Lopez, R. Lin, and C. Barrington-Leigh (2005), Terrestrial gamma-ray flashes observed up to 20 MeV, *Science*, *307*(February), 1085–1089.

Smith, D. M., et al. (2002), The RHESSI spectrometer, *Solar Physics*, *210*(1-2), 33–60, doi:10.1023/A:1022400716414.

Smith, D. M., et al. (2011), The rarity of terrestrial gamma-ray flashes, *Geophysical Research Letters*, *38*(8), n/a–n/a, doi:10.1029/2011GL046875.

Stanley, M. a., X. M. Shao, D. M. Smith, L. I. Lopez, M. B. Pongratz, J. D. Harlin, M. Stock, and A. Regan (2006), A link between terrestrial gamma-ray flashes and intracloud lightning discharges, *Geophysical Research Letters*, *33*(6), 1–5, doi:10.1029/2005GL025537.

Stolzenburg, M., W. D. Rust, and T. C. Marshall (1998), Electrical structure in thunderstorm convective regions: 2. Isolated storms, *Journal of Geophysical Research*, *103*(D12), 14,079, doi:10.1029/97JD03547.

Tavani, M., et al. (2011), Terrestrial gamma-ray flashes as powerful particle accelerators, *Physical Review Letters*, *106*(1), 1–5, doi:10.1103/PhysRevLett.106.018501.

Tierney, D., et al. (2013), Fluence distribution of terrestrial gamma ray flashes observed by the Fermi Gamma-ray Burst Monitor, *Journal of Geophysical Research: Space Physics*, *118*(10), 6644–6650, doi:10.1002/jgra.50580.

Veres, P., J. Ripa, and C. Wigger (2009), The effect of annealing on the RHESSI gamma-ray detectors, *arXiv preprint arXiv:0912.3919*.

Wilson, C. T. R. (1924), The electric field of a thundercloud and some of its effects, *Proceedings of the Physical Society of London*, *37*(1), 32D–37D, doi:10.1088/1478-7814/37/1/314.